RESEARCH ARTICLE

Control of diffuser jet flow: turbulent kinetic energy and jet spreading enhancements assisted by a non-thermal plasma discharge

N. Benard · N. Balcon · G. Touchard · E. Moreau

Abstract An axisymmetric air jet exhausting from a 22-degree-angle diffuser is investigated experimentally by particle image velocimetry (PIV) and stereo-PIV measurements. Two opposite dielectric barrier discharge (DBD) actuators are placed along the lips of the diffuser in order to force the mixing by a co-flow actuation. The electrohydrodynamic forces generated by both actuators modify and excite the turbulent shear layer at the diffuser jet exit. Primary air jet velocities from 10 to 40 m/s are studied (Reynolds numbers ranging from 3.2 to 12.8×10^4), and baseline and forced flows are compared by analysing streamwise and cross-stream PIV fields. The mixing enhancement in the near field region is characterized by the potential core length, the centreline turbulent kinetic energy (TKE), the integrated value of the TKE over various slices along the jet, the turbulent Reynolds stresses and the vorticity fields. The time-averaged fields demonstrate that an effective increase in mixing is achieved by a forced flow reattachment along the wall of the diffuser at 10 m/s, whereas mixing enhancement is realized by excitation of the coherent structures for a primary velocity of 20 and 30 m/s. The actuation introduces two pairs of contra-rotating vortices above each actuator. These structures entrain the higher speed core fluid toward the ambient air. Unsteady actuations over Strouhal numbers ranging from 0.08 to 1 are also studied. The results suggest that the excitation at a Strouhal number around 0.3 is more effective to enhance the turbulence kinetic energy in the near-field region for primary jet velocity up to 30 m/s.

1 Introduction

Among classical turbulent shear flows, axisymmetric jets are of great importance for a variety of applications such as aeronautical engine combustors or exhaust nozzles. Civil applications such as chimney stacks, chemical reactor or cooling systems are also concerned with the enhancement of jet mixing and spreading. The control of round turbulent jets exhausting in a quiescent flow was widely investigated due to the high excitability of the natural modes of instability. The boundary layer between two fluids of different velocities, temperatures or densities is naturally unstable and small perturbations imparted to the region where the large-scale structures initiate can be sufficient to significantly change the mixing properties. The improvement of the mixing characteristics of a controlled air jet usually involves different mechanisms mainly based on the manipulation of large-scale turbulent structures. The increase in mixing can consist in promoting and energizing strong streamwise vorticity which can improve the fluid transfer between the inner and outer flows. Successive merging of coherent structures (Winant and Browand 1974), the natural growth of the flow structures along the shear layer axis (Zaman and Hussain 1980) or the amplification of the natural azimuthal instabilities (Mankbadi 1985) can be involved in the overall increase in the fluid entrainment.

Many studies have demonstrated that the mixing and spreading rate of a turbulent jet can be significantly altered by applying a suitable excitation at the jet exit. Passive

N. Benard (✉) · N. Balcon · G. Touchard · E. Moreau
Laboratoire d'Etudes Aérodynamiques (LEA),
Université de Poitiers, ENSMA, CNRS,
Bld Marie et Pierre Curie, Teleport 2,
86962 Futuroscope Cedex, France
e-mail: nicolas.benard@lea.univ-poitiers.fr

control devices such as tabs can generate contra-rotating vortices pairs inducing strong streamwise vorticity that can change the vortex and turbulent structures of the jet flow and thus enhance the jet mixing (Zaman et al. 1994; Reeder and Samimy 1996). These flow structures produced in the near-field region could result in an increase of the turbulent kinetic energy in the far-field region (Bridges 2002). For instance, Zaman et al. (1994) have demonstrated that the length of the potential core of an axisymmetric jet can be shortened (the jet centreline pressure decays much faster and the length of the potential core is reduced by approximately 2 diameters with 4 delta-tabs) and that the flow modifications occur up to 6 diameters downstream the exit of axisymmetric subsonic and supersonic air jets.

As previously mentioned, the initial shear layer of axisymmetric jets is particularly sensitive to small disturbances which are amplified through their natural instability (Huerre and Monkewitz 1990). A large spreading can be achieved if proper excitation frequencies are chosen (Parekh et al. 1996). As opposed to the passive control method, active control devices are suitable for performing effective unsteady excitations. Acoustic excitations (Corke and Kusek 1993; Parekh et al. 1998), fluidic systems (Strykowski and Wilcoxon 1993; Parekh et al. 1996; Boguslawski et al. 1999; Delville et al. 2000) or MEMS (Kurimoto et al. 2005; Suzuki et al. 2004) have demonstrated their efficiency to promote the initial instabilities of axisymmetric jet flows resulting in promising improvements of the jet mixing and spreading.

Passive and active devices can be united in order to emphasize the flow control. For instance, a short diffuser attached to the exit of an axisymmetric air jet induces higher initial thickness of the shear layer but also increases the effectiveness of a suitable periodic excitation (Pack and Seifert 1999). Such configuration increases the number of parameters having consequences on the effectiveness of the control for jet deflection and mixing purposes. The diffuser attached to the jet exit allows to significantly increase the jet spreading even by applying small excitation in the region where large-scale structures initiate. Furthermore, in the case of an excitation operated in counter-flow mode, a jet extended by a small angle diffuser can promote absolute instability (Strykowski and Wilcoxin 1993). More recently, Ben Chiekh et al. (2003) studied a jet flow, naturally separated from the walls of a large angle diffuser. The synthetic jets placed in the direction of the primary flow (at the juncture between the jet exit and the diffuser) allowed to attach the flow along one lip of the diffuser. A local singular action or two simultaneous actions at opposite positions result in a jet vectoring and in a mixing increase, respectively.

Actuators based on plasma discharge technology are currently developed for a wide range of industrial purposes including the active control of airflow (Moreau 2007; Roth et al. 2007). Two plasma actuator concepts have proven their efficiency for airflow control. The first one uses the local thermal effect due to arcs discharge occurring in the inter-space of two electrodes powered by a high-voltage amplifier. Samimy et al. (2004) were the first authors to force various instabilities in free jet with an actuator based on a local high frequency heating (repetition rate up to 200 kHz) resulting in a pressure jump in the filament region. Eight electrodes were placed around the nozzle perimeter of a Mach 0.9 (Samimy et al. 2007a) and 1.3 (Samimy et al. 2007b) round jet, 1 mm upstream the exit plane. Results demonstrate that a substantial mixing enhancement is achieved if the jet is excited around its jet preferred mode (Strouhal number from 0.2 to 0.5). This range of Strouhal number (St) caused a significant reduction of the potential core (the potential core length is of about 6–8 diameters for baseline flow while the centreline velocity began to decay at 4 diameters for controlled case) and an increase in the decay rate of the centreline velocity beyond the end of potential core where the manipulated large-scale structures directly interact with the centreline region. The second category of plasma actuators consists in generating an ionized surface area above an aerodynamic wall. This ionized air region produces an electrohydrodynamic (EHD) force inducing a change in pressure distribution above a dielectric surface due to a local electric wind tangentially to the plasma surface. Corona discharges or dielectric barrier discharges (DBD) allow to create a local electric wind of a few m/s (0–8 m/s) at the dielectric surface. The velocity can be controlled by adjusting the high-voltage magnitude, the frequency and the electrode geometry (Roth and Dai 2006; Forte et al. 2007). The produced airflow can be directed in co-flow or counter-flow mode according to the geometric configuration of the electrodes. Furthermore, and contrary to local arcs, the thermal effects are not responsible for the local airflow produced by a single DBD and have no effects on the flow control process (Jukes and Choi 2006). Despite the low velocity generated by a surface plasma discharge, and due to the direct interaction within the boundary layer, lots of subsonic aerodynamic flows have been controlled using non-thermal surface plasma actuators (Corke and Post 2005; Moreau 2007). Control of axisymmetric jet was first studied by Corke and Matlis (2000) using a phased plasma arrays composed of nine DBDs placed inside a circular extension nozzle. The plasma formed in contact with the air jet (main jet velocity of about 30 m/s, Reynolds number of about 1.05×10^5) allowed to excite the helical modes m ($0 \leq m \leq 8$) via an electric wind transverse to the primary flow. The results demonstrated that the actuation induced high centreline fluctuations and that, downstream the jet exit, the excitation resulted in slightly faster centreline

velocity decay, demonstrating a small increase in mixing. Since 2007, our research group has performed new experiments concerning the control of round air jet by DBD actuations. Our recent studies involve control of axisymmetric jets equipped with small angle diffusers in order to enhance the overall effects of the control as reported by Pack and Seifert (1999). The first investigation purpose was to demonstrate that a single DBD actuator (covering 1/4 of the jet perimeter) was an effective device to perform thrust vectoring (Benard et al. 2007a). By controlling the flow separation along the diffuser wall, a jet vectoring of 13° was observed at the exit of an axisymmetric jet equipped with a 12-degree diffuser for primary jet velocity of 20 m/s ($Re_D = 6.4 \times 10^4$). The effects of an unsteady actuation on turbulence were studied in a complementary publication (Benard et al. 2007b). The spectrum analysis of the data collected by a laser Doppler velocimeter along the shear layer axis demonstrated that the large scale organization can be forced at a specific electrical frequency (up to $St = 0.8$, i.e. 320 Hz) imposed by the input signal for primary jet velocity of 20 m/s ($Re_D = 6.4 \times 10^4$). This manipulation of the large scale flow structures is presumably due to the excitation of the instability in the initial region. On the other hand, the forced flow reattachment along the diffuser wall is responsible for the shedding of flow structures at lower main jet velocities ($Re_D \approx 3.2 \times 10^4$) (Benard et al. 2008).

The ability of a DBD actuator to manipulate the flow structures promotes the idea that DBD actuators could constitute an effective device to enhance the mixing of round turbulent air jet. In the present study, an axisymmetric non-reactive air jet is controlled using two DBD actuators placed symmetrically at the surface of a 22-degree-angle diffuser. Steady and unsteady actuations are performed in order to define the most efficient excitation mode to amplify the large vortex structures and the resulting increase in mixing. The results are obtained using a particle image velocimetry system allowing to measure the two or three velocity components. The analysis is based on the flow modifications in the longitudinal and streamwise planes. Further analyses are performed by examining the turbulent kinetic energy values. The processing of the collected data in terms of vorticity allows to highlight the time-averaged results.

2 Methods

2.1 Aerodynamic configuration

Experiments are performed in a 2 m-long-circular open wind tunnel at free-stream velocities up to 40 m/s. The axisymmetric jet exit has a diameter of 72.5 mm and is attached to a circular contraction outlet (ratio of 1:64). The flow is driven by a variable frequency centrifugal fan (FEVI F18G-1R-500), and passes through a series of five fine screens with decreasing grid sizes before entering into the contraction and the jet nozzle. The jet nozzle (see Fig. 1) includes a small angle diffuser (see Fig. 2) machined in polymethyl methacrylate (PMMA). The jet nozzle is 210-mm-long and a turbulator ring, fixing the laminar-turbulent transition, is placed 200 mm upstream the exhaust of the jet.

The bevels of the diffuser are 30-mm-long (see Fig. 2c) and form a 22-degree-angle with the internal jet nozzle. The half-angle of the bevel (22°) was chosen to avoid any natural flow attachment in this region. Furthermore, Pack and Seifert (1999) have proven that the presence of such diffuser affects only the initial thickness of the jet shear layer and slightly enhances the spreading rate of the baseline flow. The use of high-voltage in a confined region requires a particular care about electrical interactions between the electrodes of the two DBDs. Here, this characteristic dictates the design of a blunt trailing edge. Indeed, the thickness of the trailing edge ($h = 9$ mm) increases the distance between the active and grounded electrodes and thus prevents the spark discharges at large amplitude high-voltage which can result in drastic damage of the experimental model. It is expected that this thickness has no consequence on the spreading rate of the naturally separated baseline flow. However, the growth rate of some controlled cases could be increased due to the larger scale vortices promoted by the thick trailing edge (Braud et al. 2004). This point will be discussed later in the paper.

In the present study, the internal diameter ($D = 50$ mm) of the nozzle (upstream the diffuser) is considered as the reference length. Four Reynolds numbers based on the internal diameter D are investigated ($Re_D = 3.2, 6.4, 9.6$
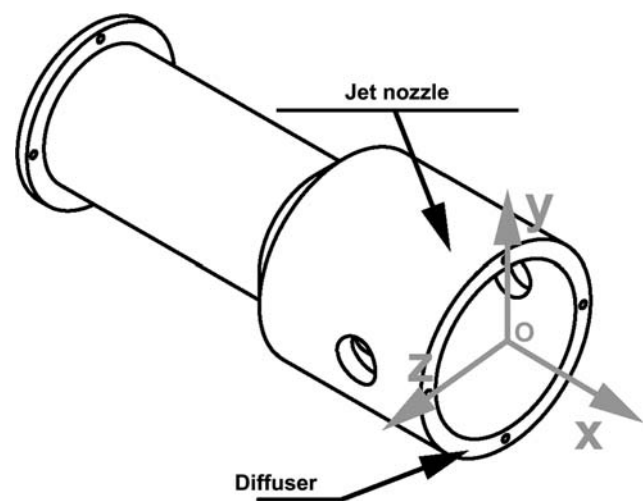

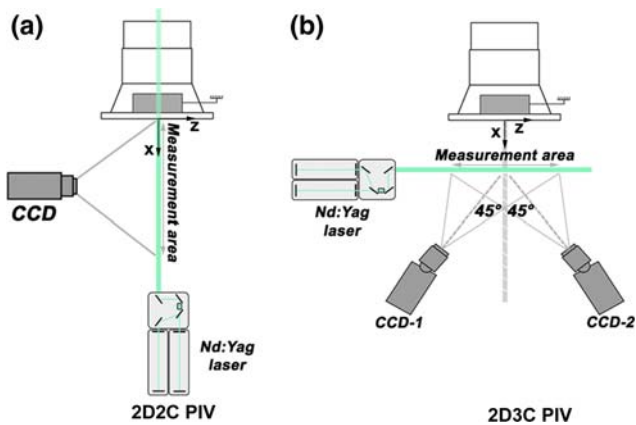**Fig. 1** Sketch of the jet nozzle exit including the diffuser

Fig. 2 Schematic of the jet nozzle diffuser, geometry and localization of the actuator

and 12.8×10^4) which correspond to primary air jet velocities (U_j) of 10, 20, 30 and 40 m/s, respectively. The time-averaged centreline velocity at the jet exit is measured with an analogical manometer (Furness, FCO14).

2.2 The dielectric barrier discharge actuator

The DBD actuator consists in two thin aluminium sheets (0.1 mm thick) separated by the wall of the nozzle exit (Fig. 2a–c, electrodes in grey). The wall acts as the dielectric and is 3-mm-thick. The electrodes are 20-mm-wide and 40-mm-long (along the internal perimeter of the jet) and the plasma discharge region is extended by the use of a small gap (5 mm) between the electrodes (Fig. 2c). Two DBD actuators are placed symmetrically on the nozzle wall in order to excite both sides of the diffuser and they cover 50% of the jet perimeter. An AC sinusoidal 40 kV_{p-p} HV is applied to the electrodes in contact with the jet and the second electrode pairs are grounded. The operating frequency is 1.5 kHz and a high-voltage power generator (Trek 30 kV/40 mA, New-York, USA) is used to amplify the sinusoidal signal generated by a digital waveform processor (TTi, TG1010A, Cambridgeshire, England).

The plasma ignition occurs when the electric field is locally sufficient to induce a pre-breakdown of the air. The charged particles present in the plasma (positive and negative ions, electrons) transfer their momentum to the neighbouring neutral particles by collisions. This momentum transfer induces a local electrohydrodynamic force, producing a flow of a few m/s located at the boundary layer. In our configuration, the produced 'electric wind' occurs in a co-flow mode presumably allowing a pressure gradient decrease along the bevels of the diffuser. According to previous measurements, this configuration ensures an ionic wind of 6 m/s located at 0.5 mm above the wall surface (Benard et al. 2007a). The velocity ratio U_{DBD}/U_j (where U_{DBD} and U_j refer to the airflow velocity produced by the actuator and the main jet velocity, respectively) at the jet exit was held at about 60 to 15% (for $Re_D = 3.2$ and 12.8×10^4, respectively). The non-thermal plasma device can operate either in a quasi-steady or unsteady manner. The quasi-steady mode consists in applying the electrical signal detailed above because the fluid response of the flow is supposed to be much lower than the AC frequency. In unsteady actuation mode, a first signal frequency is alternatively switched off and on at a lower frequency, with a duty-cycle value set to 50% (Post and Corke 2004).

2.3 Measurement facilities

Standard particle image velocimetry (PIV) and stereoscopic-PIV are used to explore the flow characteristics at the jet exhaust (maximal repetition rate of 15 Hz). Both systems are provided by Lavision company and are composed of one (for 2D2C PIV) or two (for 2D3C PIV) CCD cameras (Lavision, 1,376 × 1,040 pixels) and a Nd:Yag laser (Quantel, Twins ultra). This laser generates a 1-mm-thick sheet adjusted in the visualization plan and each laser head operates at 27 mJ per pulse. The flow is seeded with fine oil droplets ($d_{droplets} = 0.5$–$2 \ \mu m$) injected in the centrifugal fan. These seed particles result from the atomization of a pure pharmaceutical oil (Ondina 15) by a fog generator (Deltalab, EI511). The velocity components are computed using a cross-correlation algorithm with adaptative multipass, interrogation windows of 32 × 32 to 16 × 16 pixels and an overlap set to 50%. Data acquisitions in the xy plan (longitudinal acquisitions, see Fig. 3a) are realized using 2D PIV as the flow is supposed to be axisymmetric with primary air jet velocity occurring in the x direction. The camera is mounted at a distance of 0.5 m from the laser light sheet. The laser is adjusted on the centre of the couple of DBD actuators (xy plan) so that the spatial resolution of the vector fields is 1.74 × 1.74 mm (i.e. image resolution of 0.29 mm per pixel). Transverse acquisitions (yz plans, see Fig. 3b) are performed using

**Fig. 3** Diagram of the PIV arrangement for streamwise (**a**) and cross-stream (**b**) acquisitions

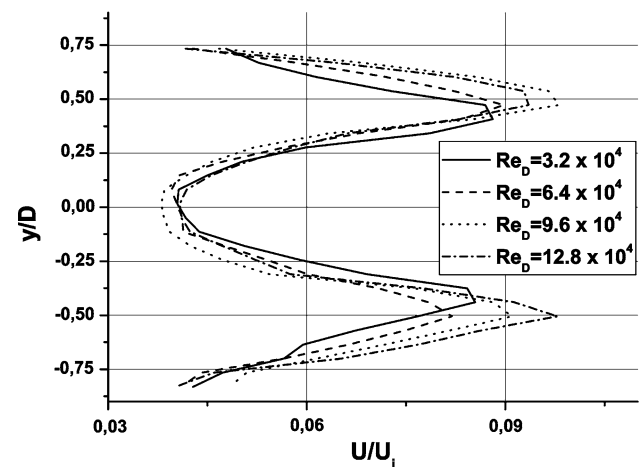**Fig. 4** Cross-stream distribution (at $z/D = 0$) of the mean velocity near the jet exit ($x/D = 0.4$) for Reynolds numbers from 3.2 to 12.8×10^4

stereoscopic PIV in backward scattering mode. The laser sheet is placed at 5 mm of the jet exit ($x/D = 0.1$) and both CCD cameras are mounted on the same side of the light sheet with an opening angle of 90° (the image resolution is 0.09 mm per pixel). This configuration is retained to capture the primary velocity component V_x with minimizing errors. The duration between two successive pulses ranges from 250 to 60 μs for Reynolds numbers ranging from 3.2 to 12.8×10^4 during the 2D2C acquisitions (these times being 90 and 22.5 μs for 2D3C measurements). The maximum particle displacement is approximately 6 pixels with a sub-pixel error of ±0.1 pixel, which corresponds to a minimal measurement accuracy of 1.15 and 0.9% in the primary velocity for 2D2C and 2D3C measurements. Time-averaged and turbulent quantities are computed from sequences of 300 instantaneous fields. A statistical analysis has demonstrated that a satisfactory convergence is achieved if a minimum of 150 instantaneous PIV fields are used to compute the mean velocity (the statistical convergence was checked along the shear layer axis and for centreline positions). The fluctuating velocity components are converged using approximately 250 PIV snapshots.

3 Results and discussions

3.1 Baseline flow

Velocity profiles near the jet exit plane ($x/D = 0.4$) are shown in Fig. 4. The normalisation is relative to the centreline velocity U_j, D is the internal jet diameter and U refers to the primary velocity component of the main jet. This figure exposes the near-field region over the whole Reynolds number range in order to characterize the baseline jet and verify the effects of the turbulator ring located a few diameters upstream the jet exit. The mean velocity profiles consist in symmetrical top-hat distributions over
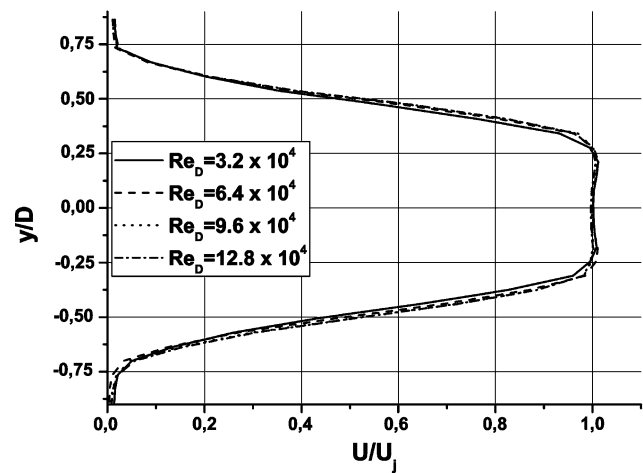
the Reynolds numbers investigated. According to the cross-stream size of the potential core (i.e. approximately $0.5D$, while the jet exit diameter is about $1.44D$), it could be expected that the initial jet flow is fully detached from the walls of the diffuser.

The cross-stream distributions of the fluctuating velocities u' close to the jet exit are presented in Fig. 5. Across $x/D = 0.4$, the relative initial turbulence intensities u'/U are symmetric with respect to the centreline axis and they present a double peak distribution. The potential core turbulence level is around 4%. As expected, the analysis of the non-dimensional fluctuating velocity indicates that the peaks of turbulence level occur in the shear layer. The locations of these peaks are nearly symmetrical and the 'initial' turbulence intensities in the shear layer remain

Fig. 5 Cross-stream distribution (at $z/D = 0$) of the fluctuating velocity u' near the jet exit ($x/D = 0.4$) for Reynolds numbers from 3.2 to 12.8×10^4

rather constant (turbulence intensity of about 8–9.5%). It is assumed that the flows are fully turbulent for every tested velocities.

The turbulent shear layer thickness ($\delta_{0.99}$) is calculated from the mean velocity profiles at $x/D = 0.2$ and corresponds to the distance at which the velocity is 99% of the core jet velocity. The results indicate that $\delta_{0.99}$ is independent of the Reynolds number ($\delta_{0.99} \approx 23$ mm). The momentum thickness of the shear layer (θ) is also measured closer to the jet exit at $x/D = 0.2$ with the following formula:

$$\theta = \int_0^\infty \frac{U(y)}{U_j}\left(1 - \frac{U(y)}{U_j}\right)dy \qquad (1)$$

At $x/D = 0.2$, for baseline flows this momentum thickness is nearly $D/17$ (increase in momentum thickness of about 12% between $Re_D = 3.2$ and 6.4×10^4, while higher Reynolds numbers present discrepancies lower than $\pm2\%$). The momentum thickness is significantly higher than usual values for a turbulent boundary layer ($D/190$) but rather close to the momentum thickness obtained by Pack and Seifert (1999). These authors obtained a momentum thickness of $D/25$ for a flow exit equipped with a 30° diffuser and a 1.85 bevel length. Furthermore, these authors have demonstrated that a significant increase in momentum thickness occurs near the jet exit (i.e. $x/D \leq 0.2$) equipped with a small-angle diffuser. Hence, it could be assumed that the initial momentum thickness is lower at $x/D = 0$.

The cross-stream mean velocity distributions from $x/D = 0.4$ up to 6 are plotted in Fig. 6. These velocities are almost constant over the Reynolds number range at each streamwise position. Figure 6 demonstrates that the centreline velocity starts to decay for streamwise position

Fig. 6 Cross-stream distribution of the mean at $z/D = 0$ for streamwise position from $x/D = 0.4$ up to $x/D = 6$. U_j denotes the maximal velocity of the main jet (i.e 10, 20, 30 and 40 m/s for $Re_D = 3.2$, 6.4, 9.6 and 12.8×10^4, respectively)
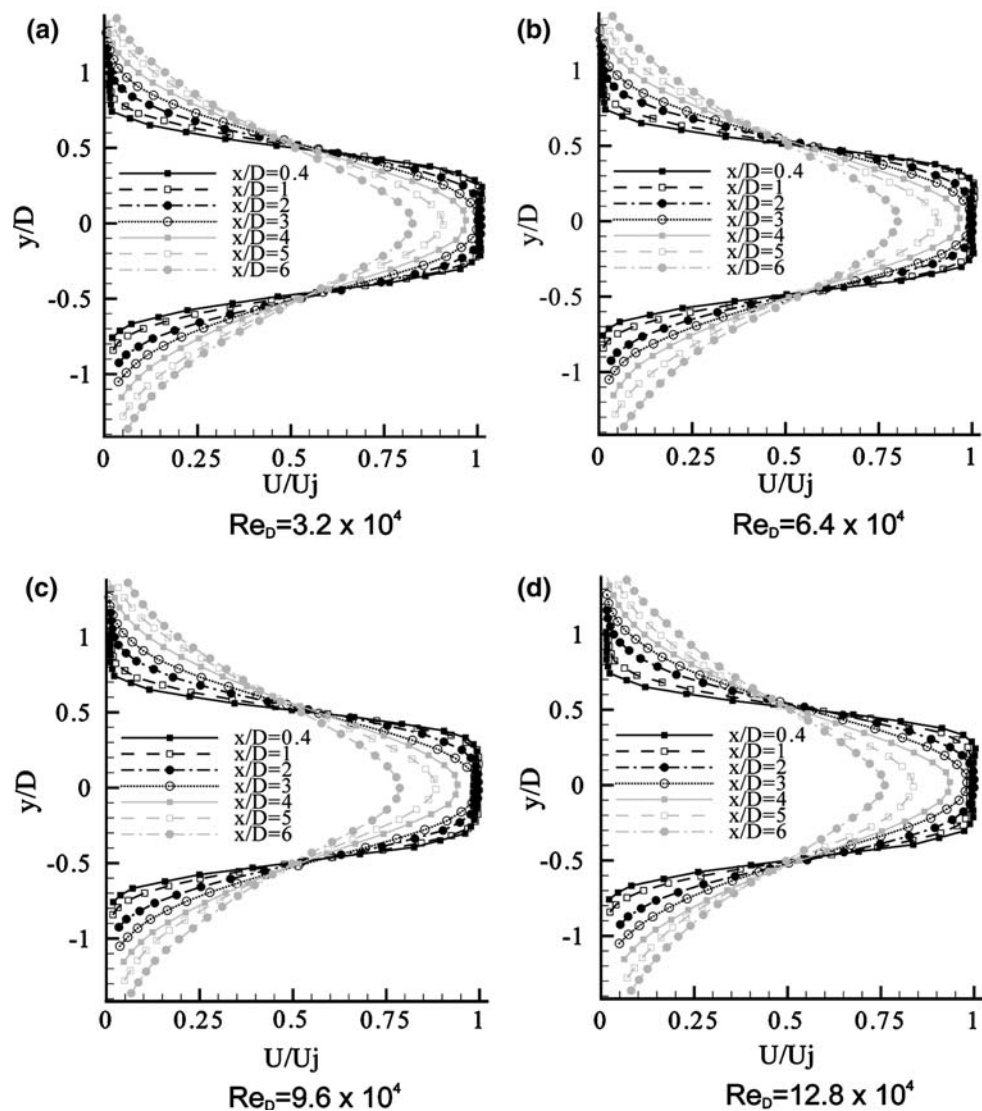
greater than $x/D = 3$. Figure 7 represents the widths of the jet based on the cross-stream locations at which the streamwise velocity U is half of the centerline value. The width linearly increases with the streamwise position regardless of the Reynolds number. According to the maximal difference of 7% in the jet widths (the difference in the slopes are lower than 2%), we can assume that the width of the jets is almost independent of the Reynolds number. Furthermore, the positive slope of the jets width in the region beyond the end of the potential core is about 0.12, which is larger than the slope value observed for conventional canonical airjet. Indeed, Hussein et al. (1994) reported that the width of a round jet linearly increases with a positive slope of 0.094 for Reynolds number around 9.5×10^4. Thus, it appears that the diffuser combined with the turbulator ring induce some modifications of the baseline jet.

The turbulator ring ensures an initial turbulent boundary layer. Consequently, the characteristics of the baseline flow may differ from the literature but it is essential to ensure that the forced flow perturbations are only due to the DBD actuators and not due to a forced transition from laminar to turbulent. According to Raman et al. (1989), the core turbulence level has no effect on the jet mixing for natural flows with a turbulent boundary layer but the control effects diminish as the initial boundary layer gets fully turbulent. Nevertheless, practical flows exhibit fully turbulent boundary layers and high core turbulence levels. Hence, it seems more important to study such flows even if the resulting effects are less effective.

3.2 Quasi-steady actuation: streamwise acquisition plane

In this section, the flow topology resulting from the modification of the cross-stream velocity profiles (at $z/D = 0$) is introduced for streamwise positions at $x/D = 0.4$, $x/D = 4$ and $x/D = 6$.
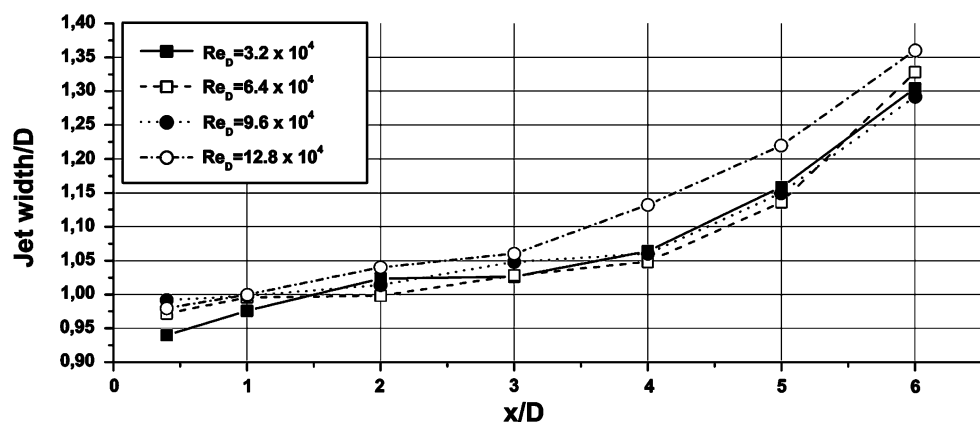
The results shown in Fig. 8 demonstrate that the most effective flow control is obtained at the lowest Reynolds number. In this flow regime, the jet is strongly affected by the DBD actuation. In the near-field region (Fig. 8a), the mean velocity profile is widely expanded in the y direction at $z/D = 0$ inducing a strong centreline velocity decay further downstream (Fig. 8b,c). At $x/D = 0.4$, it seems that the actuation has no effect on the mean velocity profiles compared to the baseline jet for Reynolds numbers greater than 3.2×10^4. However, the results further downstream highlight that a small cross-stream expansion of the forced jet is achieved even at the highest Reynolds number tested (Fig. 8c). Furthermore, the mean velocity profiles show a small decrease in the centreline velocity.

A global view of the effects of a DBD actuation on the time-averaged velocity fields (xy plan, up to $x/D = 8$) is introduced in Fig. 9 in the plane $z/D = 0$. The iso-values of the velocity norms, based on primary U and second velocity V components, are plotted in Fig. 9 for each Reynolds number tested. This norm is calculated according the following expression:

$$U_{\mathrm{norm}} = \sqrt{U^2 + V^2} \tag{2}$$

The baseline jet (coloured background in Fig. 9) is symmetrical relative to the x axis and presents a self-similar distribution along the x direction due to the initial turbulent boundary layer. As a result of the double DBD actuation (black lines in Fig. 9), major macroscopic changes in the flow appear for a primary air jet of 10 m/s (Fig. 9a). In this case, the results clearly confirm that the flow is now fully attached along the diffuser bevel. Few millimeters above the bevel, the ionic wind creates a small pressure decrease (Roth et al. 1998) which contributes to the forced flow reattachment of the naturally separated flow. The width of the jet is also largely increased in the first diameters (Fig. 10). The width linearly increases and results in a gain in width of about 62 and 165% at $x/D = 0.4$ and 6, respectively. According to Dziomba and Fiedler (1985), it could be assumed that the blunt trailing
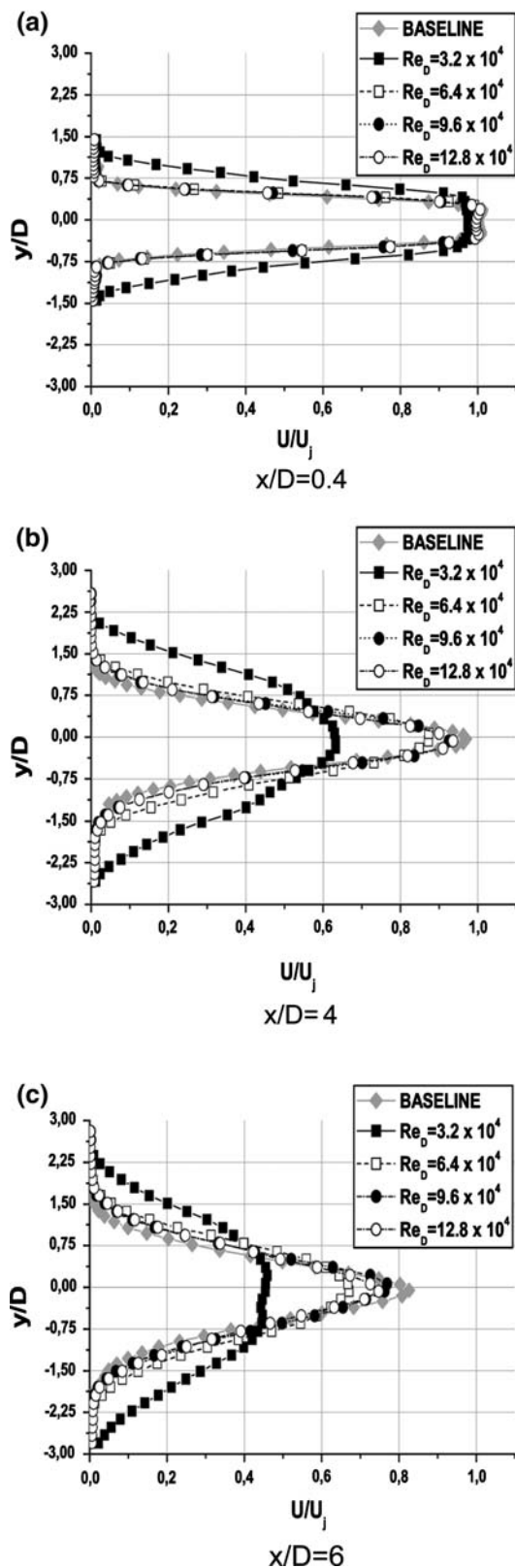
Fig. 7 Streamwise distribution of the width of the jet for baseline flows from $x/D = 0.4$ up to $x/D = 6$

Fig. 8 Cross-stream mean velocity profiles at $x/D = 0.4$, 4 and 6 for baseline and forced flows ($z/D = 0$)

edge of the diffuser could significantly affect the spreading rate of the forced jet flow. Indeed, for this Reynolds number, the controlled flow is fully attached along the wall of the diffuser. A thick, rather than a thin trailing edge could enhance the formation of large-scale structures (Braud et al. 2004). For a fully attached airflow, a small decrease of the spreading rate could be expected with a diffuser having a thinner trailing edge.

For air jets from 20 to 40 m/s (Fig. 9b–d), the EHD forces created by the plasma are too weak to force the flow reattachment, but the jet presents a slight increase in width, for velocity up to $U_j = 40$ m/s. Indeed, at $Re_D = 6.4 \times 10^4$, the jet width is increased up to 58% in the far-field region (i.e. $x/D = 6$) while at higher Reynolds numbers only a 25% maximal width gain is observed (Fig. 10).

Given the modification of the jet width, it is suspected that the actuation also leads to a change in the vorticity thickness (δ_ω). In the present study, the vorticity thickness is calculated on both sides of the potential core region and is expressed as follows:

$$\delta_\omega = U_j/(\partial U/\partial y)_{max} \qquad (3)$$

The streamwise evolution of the vorticity thickness at $z/D = 0$ is plotted in Fig. 11. Here again, the results demonstrate that the actuation is particularly effective at $Re_D = 6.4 \times 10^4$. Indeed, at 10 m/s, the vorticity thickness is increased by 132 and 142% at $x/D = 0.4$ and 1, respectively ($\delta_\omega = 0.62D$ and $1.45D$ for baseline and forced flow at $x/D = 0.4$, for instance). At higher Reynolds number, the actuation creates a vorticity region in the core zone thicker than for the baseline flow. Moreover, this increase is nearly constant (around 15%), regardless of the Reynolds number.

3.3 Quasi-steady actuation: cross-stream acquisition plane

The iso-contours of the velocity norm [see Eq. (2)] in the cross-stream visualization plane (yz plan at $x/D = 0.1$) are plotted in Fig. 12. As expected, the baseline cross-stream fields show an axisymmetric and self-similar distribution, spreading in concentric circles of uniform velocity. During the actuation, the flow at $U_j = 10$ m/s (Fig. 12a) is deflected towards the bevels where the actuators take placed. The jet cross section contracts in the z direction and expands in the y direction. For a primary velocity of 20 m/s (Fig. 12b), the flow remains moderately elongated whereas for a velocity of 30 m/s (Fig. 12c), the deformation only occurs in the outer part of the round jet. At 40 m/s (Fig. 12d), the actuation has a low effect on the cross-stream velocity distribution.
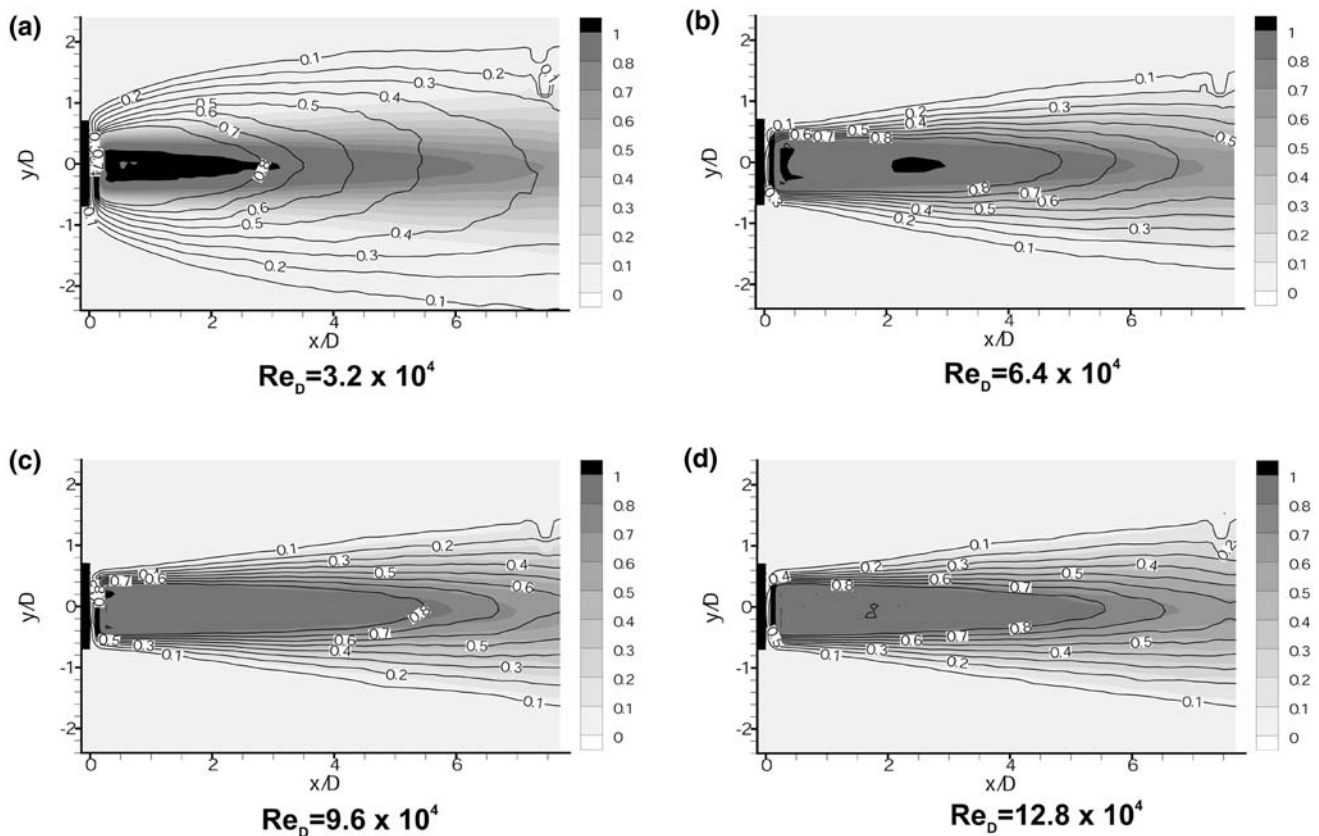
Fig. 9 Time-averaged velocity norms for the streamwise plane ($z/D = 0$). The velocities are normalized by the main jet velocity U_j. The *black lines* denote the forced flow while the background is *coloured* by the baseline flow
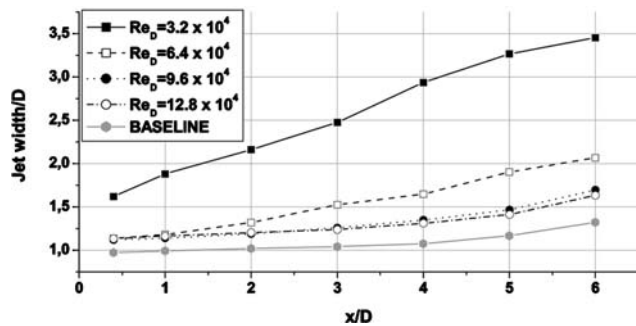

Fig. 10 Streamwise distribution of the width of the jet for forced (*black symbols and lines*) and baseline (*grey symbol and line*) flows from $x/D = 0.4$ up to $x/D = 6$ at $z/D = 0$

Fig. 11 Streamwise distribution of the vorticity thickness (δ_ω) of the jet for forced and baseline flows from $x/D = 0.4$ up to $x/D = 6$

3.4 Quasi-steady actuation: characterization of the mixing enhancement

Two classical quantities are used to evaluate the mixing enhancement occurring under actuation. The first parameter is related to the jet centreline decay along the x axis where a large drop in velocity (between the natural and forced flow) presumably confirms an increase in mixing. The second parameter is the turbulent kinetic energy (TKE)

which is the mean kinetic energy associated to the eddy structures. The instantaneous values of TKE can vary substantially, so it is useful to compute a mean TKE values, which are more representative of the overall flow. This turbulent statistic can be approached by the following expression in 2D flows:

$$\text{TKE} = \frac{\frac{1}{2}\left(\overline{u'^2} + \overline{v'^2}\right)}{U_j^2} \tag{4}$$

where u' and v' denote the primary and secondary components of the fluctuating velocity according to the

(a)

$Re_D = 3.2 \times 10^4$

(b)

$Re_D = 6.4 \times 10^4$

(c)

$Re_D = 9.6 \times 10^4$

(d)

$Re_D = 12.8 \times 10^4$
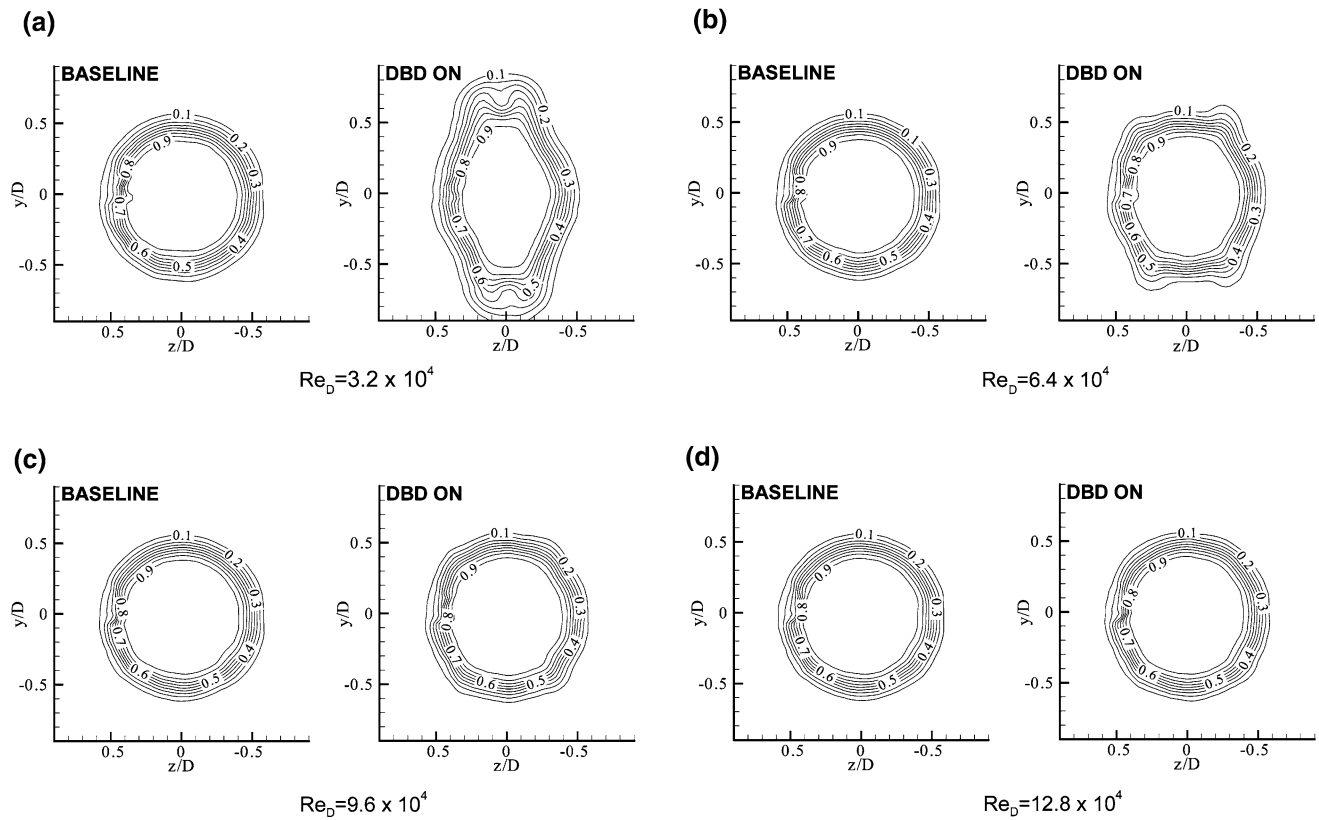
Fig. 12 Front view of the time-averaged velocity norms in transverse plane at $x/D = 0.1$

referential used in the present study. It is expected that the natural and forced flows are highly 3D and thus the computation of the TKE based on three velocity components can vary. Indeed, it is expected that the expression given in (4) will result in a lower TKE value compared to the TKE computed on the three fluctuating velocity components. A brief comparison based on the stereo-PIV fields has demonstrated that the shapes of the TKE profiles at $x/D = 0.1$ are similar but the levels of the peaks of turbulent energy can be underestimated by 15 to 35% (at $Re_D = 12.8$ and 3.2×10^4, respectively).

The jet centreline velocity developments along the x axis for the excited and baseline cases are plotted in Fig. 13. The jet centreline velocity is relatively constant inside the potential core of the jet and the baseline centreline evolutions are similar. As the shear layers merge toward the center, the centreline velocity decreases downstream. In the present study, the potential core is defined as the distance from the nozzle exit to the point where the axial velocity has decreased of 99% relative to the initial axial velocity. The end of the potential core for baseline flows can be observed near $x/D = 3.2$–3.5. The potential core is then shorter than previously reported data about the length of a canonical jet. However, if we add the length of the

separated region upstream of the exit plane (i.e. $D/2$), we obtain a total length of the potential core of approximately 3.7–4D, which is in agreement with results published by Hussein et al. (1994) or Mi et al. (2000) among others. Moreover, downstream of the potential core region, the decay of U is usually approximated by the expression:

$$\frac{U}{U_j} = K \frac{D}{x - x_p} \tag{5}$$

where x_p is the virtual origin and K the dimensionless mean velocity decay constant. Here, if we use equation (5) to approximate the decay of the unforced velocity beyond the end of the potential core (here $x/D > 4$ is chosen), we find $K \approx 6.8 \pm 0.5$ with $x_p \approx -2.3 \pm 0.5D$, these values being consistent with previous experimental and numerical investigations (Malmström et al. 1997; Lardeau et al. 2002).

Under actuation, the potential core is reduced for primary jet velocity up to 30 m/s (Fig. 13a–c). At 40 m/s, the difference in jet centreline decay is not significant (Fig. 13d). According to the jet decay observed in Fig. 13, the potential core is reduced by 45, 32 and 10% for primary velocity of 10, 20 and 30 m/s, respectively (Fig. 6a–c). One can remark that the rate of the centreline velocity

Fig. 13 Centrelines velocity evolution along the *x* axis for baseline (*solid lines*) and forced (*dashed lines*) flows
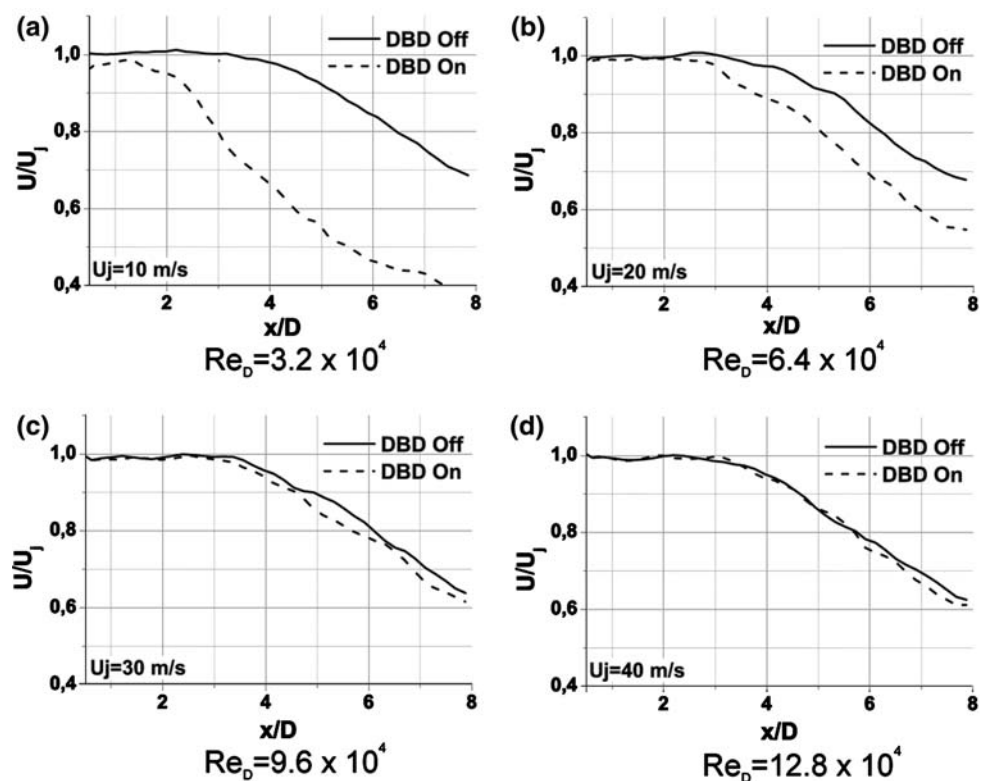
decay remains nearly constant for jets at Reynolds numbers of 9.6 and 12.8×10^4 (the mean velocity decay constant K is 5.9 ± 0.5 and x_p is about $-1.7 \pm 0.7D$). At lower Reynolds numbers, the decay constant K is largely reduced (4 and 4.5 at $Re_D = 3.2 \times 10^4$ and 6.4×10^4, respectively). These observations are presumably due to the fact that the flow does not reattach on the bevel diffuser for Reynolds numbers higher than 6.4×10^4 and thus a higher velocity is maintained in the potential core. In these cases, the jet decay could be only governed by the control of the initial shear layer at the internal beginning of the diffuser, contrary to the observations made for the lowest speed jet velocity for which the forced reattachment has an important contribution to the mixing enhancement.

The centreline evolution of the TKE values along the streamwise direction is plotted in Fig. 14 for excited and unexcited flows. For the baseline flows, the centreline TKE value increases with the axial location and the positive slope of the curves increases with the primary air jet velocity. Under excitation and Reynolds numbers of 3.2×10^4 and 6.4×10^4 (Fig. 14a, b), the TKE increases until a first threshold of 0.028 is reached and decreases further downstream. The axial position of the threshold is shifted with the primary jet velocity (threshold occurring at $x/D = 4.1$ and 5.8 for Reynolds numbers of 3.2×10^4 and 6.4×10^4, respectively). The turbulent energy in the center of the axisymmetric jet is increased compared to baseline

flows up to 5.5 and 6.5 diameters for velocities of 10 and 20 m/s, respectively (Fig. 14a, b). Further downstream, the energy initially imparted by the actuator may dissipate more rapidly and thus the TKE of the forced jets becomes lower than in the baseline case. Lardeau et al. (2002) have reported similar results by direct numerical simulation computation and they interpret this energy decay as a possible spatial redistribution of the energy in the far-field region due to the highly three-dimensional character of the mean flow. There is no noticeable overall enhancement of the turbulent energy in the round jet centreline at $Re_D = 9.6 \times 10^4$ and 12.8×10^4 (Fig. 14c, d).

The analysis of the centreline value of the TKE may not be sufficient to completely characterize the global modifications resulting from the DBD actuation. In order to represent the whole flow over the *y* direction, the integrated values of the TKE (k_int) along slices ($x/D = 1–7$, at $z/D = 0$) are shown in Fig. 15. The integrated values of the TKE at each axial position are calculated using:

$$k_\mathrm{int} = \int\limits_{-\infty}^{\infty} \frac{1}{2}\left(\overline{u'^2} + \overline{v'^2}\right)\mathrm{d}y \qquad (6)$$

As mentioned for the expression used for computing TKE, it is expected that k_int is underestimated compared to the TKE calculated from the three fluctuating velocities. In the present study at $x/D = 0.1$ and $z/D = 0$, the

Fig. 14 Effects of the actuation on the centreline evolution of the TKE for baseline (*solid lines*) and forced (*dot lines*) flows
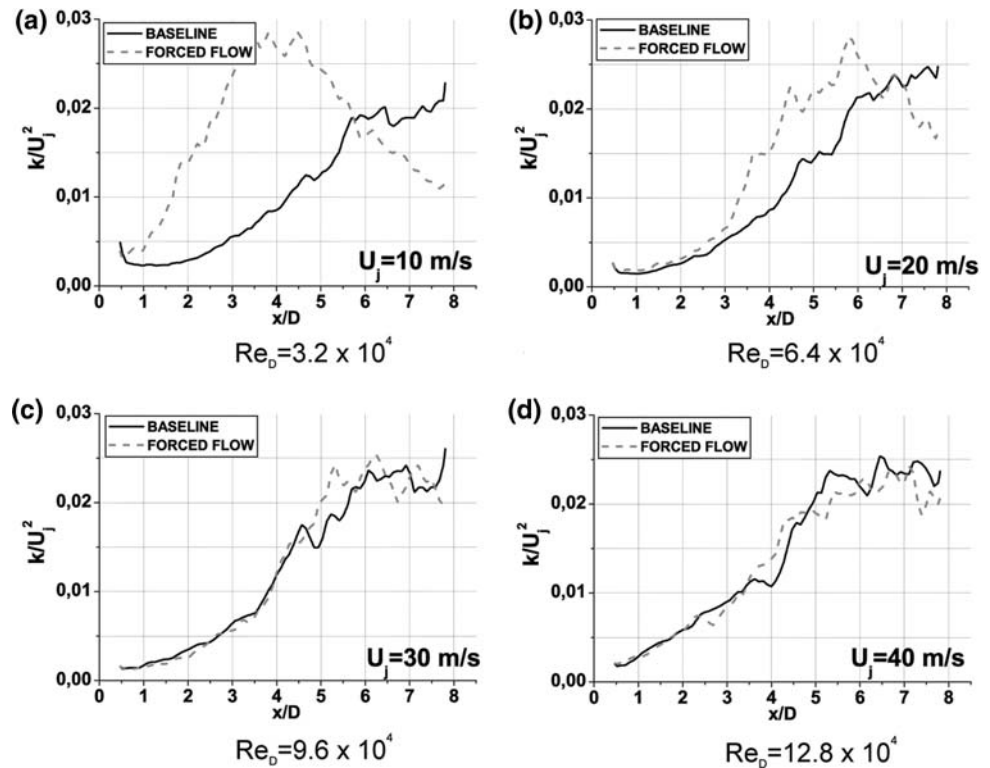
underestimation k_{int} values is about 20, 24, 28 and 35% for $Re_D = 12.8, 9.6, 6.4$ and 3.2×10^4, respectively.
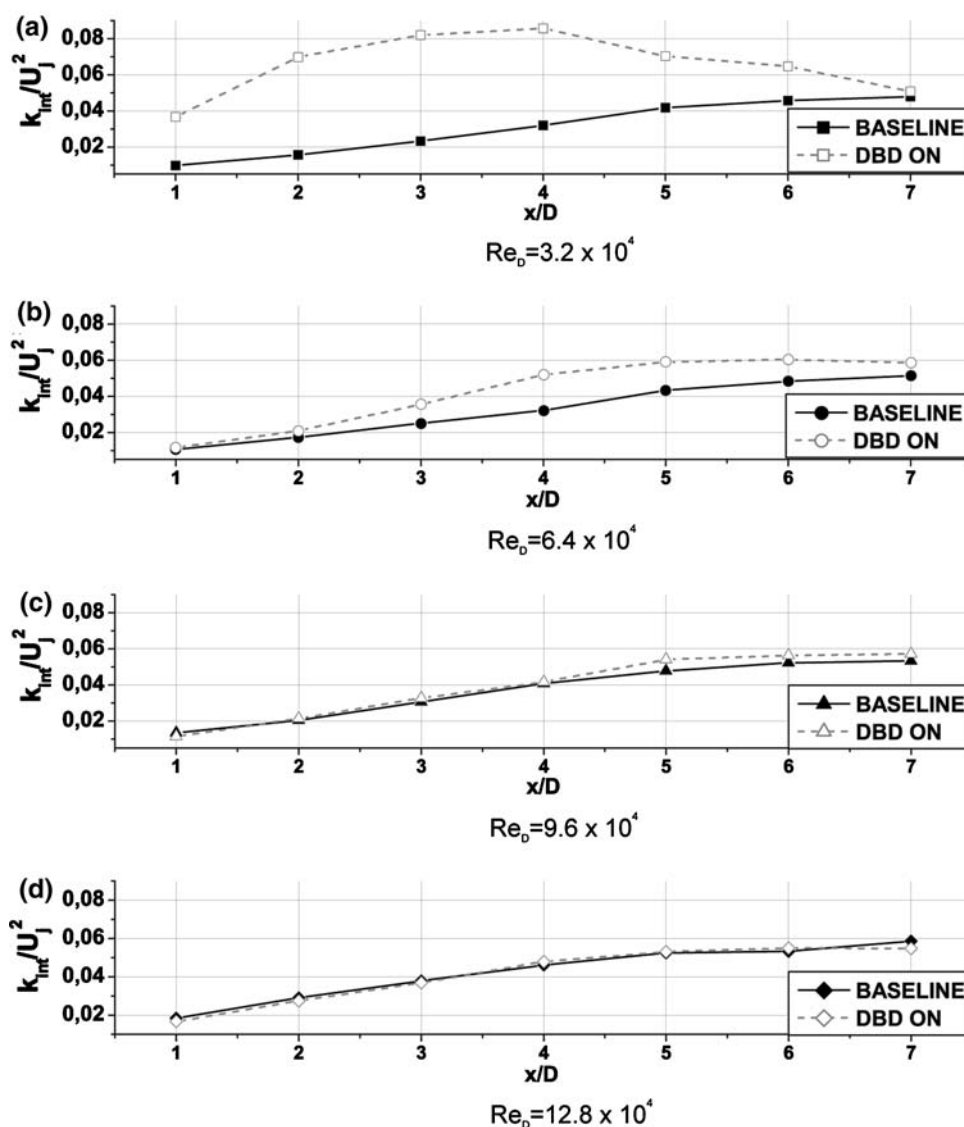
Figure 15 demonstrates that the integrated TKE for baseline flows exhibits a similar shape at each Reynolds number investigated. The TKE linearly increases up to $x/D = 5$ (positive slope of about $8.3 \pm 0.4 \times 10^{-3}$) and then the slope of the TKE curve slightly decreases (positive slope of about $3 \pm 0.5 \times 10^{-3}$). However, the TKE values of the baseline flow exhibit an increase of turbulent energy in respect with the Reynolds number.

The results demonstrate that for Reynolds numbers up to 6.4×10^4 (Fig. 15a, b), the excited flow has a higher level of integrated TKE than baseline flow over the whole range of x/D. Indeed the maximal gain in TKE is 160 and 60% (at $x/D = 4$) for $Re_D = 3.2$ and 6.4×10^4, respectively. However, at $Re_D = 6.4 \times 10^4$ (Fig. 15b), the gain in integrated TKE is only effective for positions upstream $x/D = 2$ as numerically observed by Lardeau et al. (2002) for jet flow controlled by fluidic injection. Contrary to the TKE value along the centreline axis, the integrated TKE level at 30 m/s ($Re_D = 9.6 \times 10^4$, Fig. 15c) is greater than the baseline flow starting from the position $x/D = 4$ (TKE gain of 10% at $x/D = 5$). The discrepancy between centreline TKE values (Fig. 14c) and integrated TKE over the y direction (Fig. 15c) is not surprising. Indeed, it could be expected

that the major change in the flow organization occurs in the shear layer regions as the actuation is performed in the zones where the shear layer initiates. As demonstrated by the results plotted in Fig. 14, the flow control of the centreline region is only significant at low velocity (i.e. $Re_D \leq 6.4 \times 10^4$, Fig. 14a, b). However, as demonstrated by Fig. 15, the DBD actuation can produce a small increase of the integrated TKE at $Re_D = 9.6 \times 10^4$ in the far-field region and the width of the jet at $z/D = 0$ is slightly increased for this Reynolds number (Fig. 10). These results demonstrate that a potential enhancement of the mixing using our configuration seems to be limited to Reynolds numbers lower than 12.8×10^4.

The contribution of the turbulent energy in the x and y directions can be decomposed by computing the turbulent Reynolds stresses components $\overline{u'u'}/U_j^2$, $\overline{v'v'}/U_j^2$ and the non-diagonal term $\overline{u'v'}/U_j^2$ representing the turbulent viscosity. Such quantity is a relevant parameter that highlights the momentum transfer due to the random turbulent fluctuations. The computation of the turbulent Reynolds stresses for baseline flows reveals that the $\overline{u'u'}/U_j^2$ component is the main source of turbulent kinetic energy (Fig. 16). Moreover, the rise in turbulent kinetic energy observed in Fig. 15 when the Reynolds number is increasing appears to be related to an increase of both diagonal terms (i.e. $\overline{u'u'}/U_j^2$ and $\overline{v'v'}/U_j^2$). Conversely, the

Fig. 15 Integrated value of the TKE along slices at $x/D = 1$ to 7 and $z/D = 0$

(a) k_{int}/U_j^2

BASELINE
DBD ON

$Re_D = 3.2 \times 10^4$

(b) k_{int}/U_j^2

BASELINE
DBD ON

$Re_D = 6.4 \times 10^4$

(c) k_{int}/U_j^2

BASELINE
DBD ON

$Re_D = 9.6 \times 10^4$

(d) k_{int}/U_j^2

BASELINE
DBD ON

$Re_D = 12.8 \times 10^4$

non-diagonal term of the turbulent Reynolds tensor remains constant over the investigated Reynolds number range.

The DBD actuation leads to a significant increase of the turbulent Reynolds stresses up to $Re_D = 9.6 \times 10^4$, as previously deduced from the TKE computations (Fig. 17a–c). In particular, the terms of the turbulent Reynolds tensor are increased in the near-field region ($x/D < 4$) at low Reynolds number (Fig. 17a) while at higher Reynolds number (up to $Re_D = 9.6 \times 10^4$, see Fig. 17b,c) the changes in turbulent Reynolds stresses occur in the far-field region ($x/D > 4$). At $Re_D = 12.8 \times 10^4$ (Fig. 17d), the three components of the tensor remain unchanged unlike the baseline flow at a same centreline jet velocity. Once again, the increase in TKE seems to be related to the significant variations of $\overline{u'u'}/U_j^2$.

3.5 Quasi-steady actuation: vorticity production

This section is dedicated to the analysis of the change in large-scale structures in order to interpret and explain the time-averaged fields, the centreline velocity decays and the TKE distributions. The mean streamwise vorticity ω_x of the cross-stream PIV fields is computed from the stereo-PIV acquisitions in order to characterize the flow vortices produced by the actuation. The vorticity ω_x is expressed in its dimensionless form as follows:

$$\omega_x = \frac{D\left(\frac{\partial W}{\partial y} - \frac{\partial V}{\partial z}\right)}{U_j} \tag{7}$$

where W is the third velocity component of the jet flow. It is expected that the interaction between the main jet flow
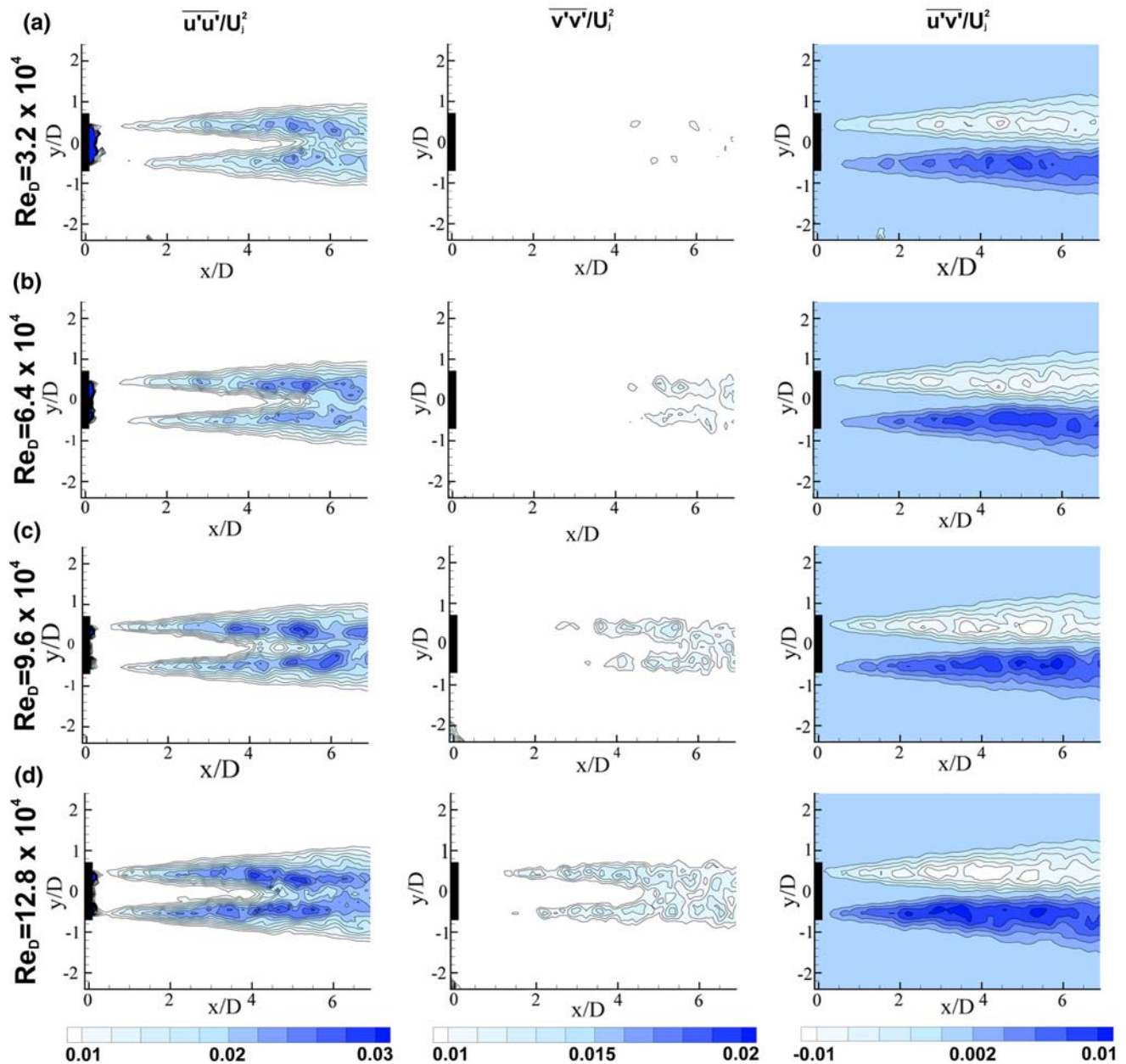
Fig. 16 Turbulent Reynolds stresses in the streamwise PIV fields at $z/D = 0$ for baseline flows

and the electric wind promotes the production of streamwise vorticity.

Figure 18 introduces the mean vorticity distribution over the jet cross sectional plane at a distance of 0.1 diameter of the nozzle exit. We remark that the mean vorticity in the shear layer remains low in the baseline case without regions presenting high vorticity (Fig. 18a, c, e, g). However, the natural flow presents a pair of small vortices in the middle left of the axisymmetric jet ($y/D = 0$, $z/D \approx 0.5$). These vortices are simply due to the electrical connections necessary to power the active

electrode. Nevertheless, the mean vorticity field for baseline flow suggests an homogeneous growth of the vortex structures in the x direction. At Reynolds numbers of 3.2 and 6.4×10^4 (and in some case at $Re_D = 9.8 \times 10^4$, see Fig. 18f), four regions with streamwise vortices pairing emerge at the lateral edge of the electrodes (regions i, j, k, l in Fig. 18b, d). The direction of rotation of each pairs of vortices is such that there is an ejection of the jet core fluid into the ambient flow like flow structures downstream tabs (Reeder and Samimy 1996; Mi and Nathan 1999). These vortex pairs
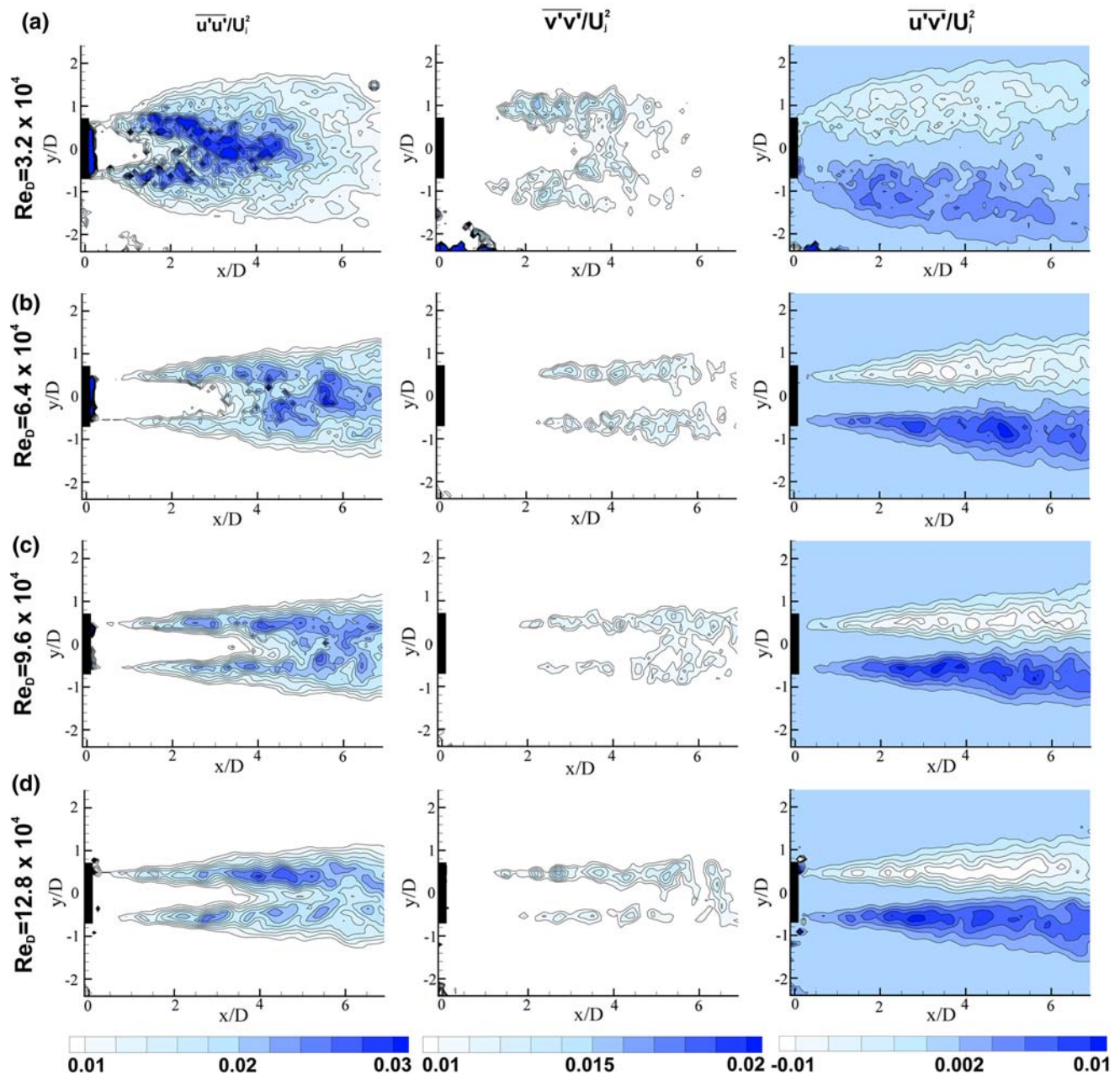
Fig. 17 Turbulent Reynolds stresses in the streamwise PIV fields at $z/D = 0$ for forced flows

are initiated by the interaction between the main jet and the electric wind and are formed in the skewed shear layer region. The central contra-rotating vortices ($z/D \approx 0$ and $y/D \approx \pm 0.7$ in Fig. 18b) have a larger vorticity intensity than the surrounding vortices and they are presumably initiated by the local pressure decrease occurring in the plasma region along the diffuser wall. This local pressure gradient could induce a full or partial flow reattachment resulting in streamwise vortices as previously observed by different authors for jet flow control by tabs (Zaman and Raman 1997; Foss and Zaman 1999) or fluid injection

(Lardeau et al. 2002). In fact, the two plasma discharges enhance the momentum transfer towards the upper and lower boundary layers ($y/D \approx 0.5$, $z/D \approx 0$) along the diffuser wall as demonstrated by the velocity fields in the transverse planes (Fig. 12). The flow structures are stretched towards the wall of the diffuser and form two quasi-steady streamwise tubes of vorticity. The external vortices result from the interaction between the controlled jet and the external quiescent flows. These flow structures are larger than the central ones but their intensity remains weaker.
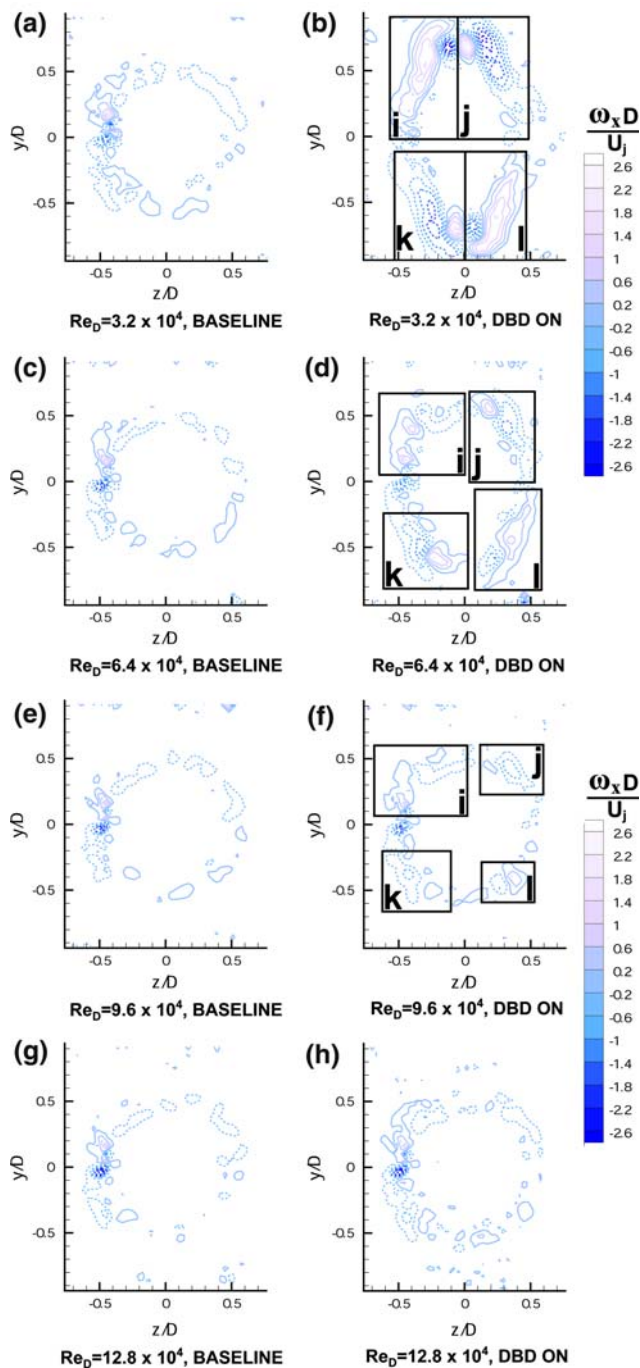
Fig. 18 Front view of the mean streamwise vorticity ω_x at $x/D = 0.1$. The *solid lines* and the *dotted lines* correspond to the positive (*counter-clockwise*) and negative vorticity (*clockwise*) values, respectively

In Fig. 18b and d, the two upper vortex pairs (i and j) eject the jet core fluid in the same positive y direction contrary to the two lower vortex pairs (k and l) which eject flow in the negative y direction. The elongation of the jet cross section may result from the presence of these vortex pairs. For the highest velocity (Fig. 18h), the vortex dynamic induced by actuation could not be confirmed.

Table 1 Unsteady excitation frequencies and corresponding Strouhal numbers

f (Hz)	50	100	150	200	300	400
St 20 m/s	0.125	0.25	0.375	0.5	0.75	1
St 30 m/s	0.08	0.16	0.25	0.33	0.5	0.66

The jet centreline decay and the consecutive increase in mixing previously identified in the time-averaged data can be explained by the characteristics of the mean streamwise vorticity. Up to $Re_D = 9.6 \times 10^4$, the core jet ejection may enlarge the cross-stream section of the round jet. Moreover, such flow ejection associated with pairs of contra-rotating vortices may result in two vortex pairs moving away from each other along the z direction due to their mutual induction (Lardeau et al. 2002). It is expected that these observations will be confirmed by acquisitions along the x direction (up to the position where the flow recover an axisymmetric behaviour). However, these planes of investigations were not acquired in the present study. A last observation concerns the vortex pairs, which are symmetrically located along the z axis. This suggests that the flow change due to the control could be more significant at positions differing from $z/D = 0$, especially at intermediate Reynolds numbers.

3.6 Unsteady actuation: characterization of the mixing enhancement

To optimize the forcing, it is necessary to develop an efficient unsteady actuation. Indeed, an unsteady actuation at an appropriate frequency can change the mixing with more effectiveness than a quasi-steady actuation. Furthermore, unsteady excitations are performed with a duty-cycle (here, fixed to 50%) which decreases the power consumption of the control device. In the present study, six excitation frequencies (f) are investigated (50, 100, 150, 200, 300 and 400 Hz). The results for primary air jet velocity of 20 and 30 m/s are presented. The Strouhal number is expressed as: $St = \frac{f \cdot D}{U_j}$ and the Strouhal numbers associated with the frequency range tested are summarized in Table 1.

In this section, the effects of the excitation frequency are measured by comparing the mean and fluctuating velocity profiles at different streamwise positions. The increase in mixing is evaluated from the changes in centreline decay, centreline TKE distribution and evolution of the integrated TKE values over the range of St values investigated.

The cross-stream distribution of the mean velocity at three streamwise positions is plotted in Fig. 19 for

Fig. 19 Cross-stream mean velocity profiles ($z/D = 0$) at $Re_D = 6.4 \times 10^4$ for excitation at Strouhal number from 0.125 up to 1
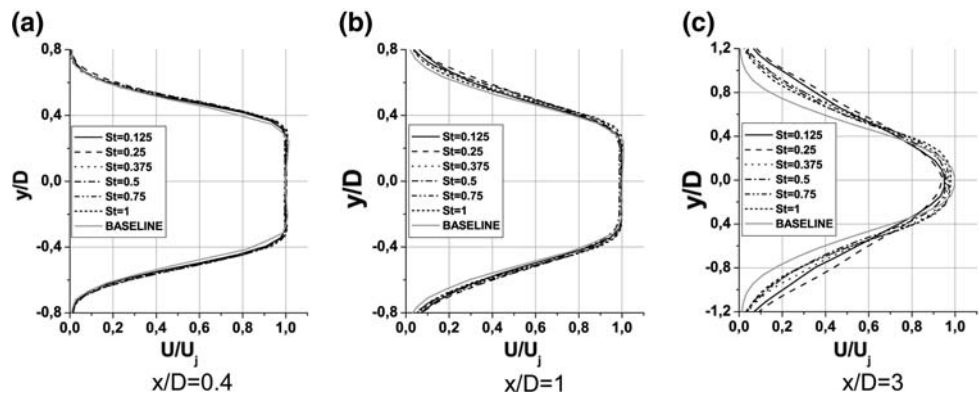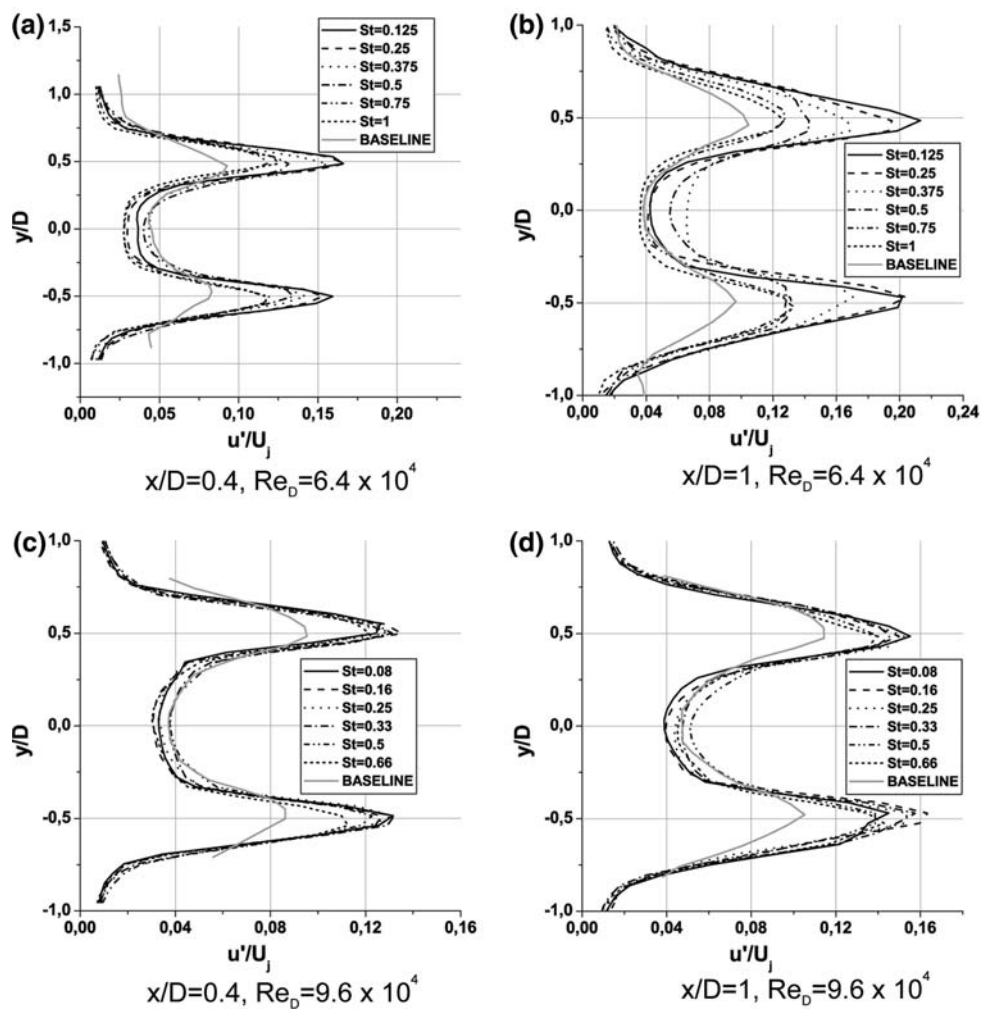

Fig. 20 Frequency effects on the cross-stream fluctuating velocity ($z/D = 0$) at $Re_D = 6.4 \times 10^4$ (**a, b**) and $Re_D = 9.6 \times 10^4$ (**c, d**)

$Re_D = 6.4 \times 10^4$. The effects of the frequency remain weak in the near field region (Fig. 19a) while the effects are improved in the region close to the end of the potential core (Fig. 19c). It appears that an excitation at a Strouhal number of 0.25 is the most effective unsteady actuation for

this Reynolds number. The resulting profiles exhibit a jet width increase (maximal jet width gain of about 19%) and a decrease of the centreline velocity (decrease of about 4%) greater than those obtained with other frequencies (Fig. 19c). At $Re_D = 9.6 \times 10^4$, the results are similar
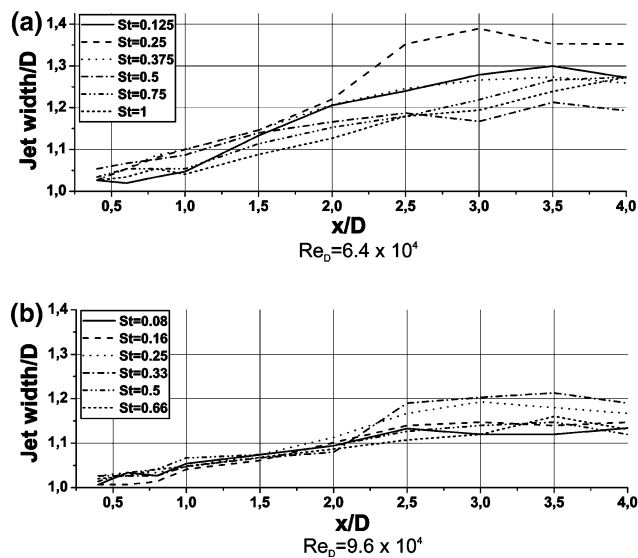
Fig. 21 Jet width ($\delta_{1/2}$) evolution with the Strouhal number at $U_j = 20$ m/s (**a**) and 30 m/s (**b**)

Fig. 22 Comparison of the centreline velocity decay for baseline and flow forced by a steady and optimized unsteady actuation

apart from the optimized unsteady excitation which is achieved at a slightly higher Strouhal number (about 0.33). According to Fig. 20, it appears that $St = 0.25$ and 0.33 correspond to an increase of the turbulent intensity along the shear layer axis while the centreline fluctuating velocities remain weak.

The width of the jets ($\delta_{1/2}$) is measured and plotted in Fig. 21. As previously mentioned this quantity is defined as the radial position where the mean velocity is $U_j/2$. This figure confirms that the effects of the frequency are enhanced in the far field region (i.e. $x/D > 2$) while the near field region is not affected by the excitation frequency imposed by the DBD actuator. As demonstrated with the mean velocity profiles, the most effective unsteady actuation is performed for Strouhal numbers of 0.25 and 0.33 at $Re_D = 6.4$ and 9.6×10^4, respectively. Crow and Champagne (1971), and Hussain and Zaman (1981) found that the preferred mode corresponds to a Strouhal number of 0.3. It corresponds to the frequency of the vortices at the end of the potential core (jet column mode). An actuation around this frequency has previously enhanced the mixing of turbulent axisymmetric jets excited by arc discharges ($St = 0.3$, Samimy et al. 2004) and MEMS ($St = 0.25$, Suzuki et al. 2004), for instance. According to Raman et al. (1989), the frequency of the most effective excitation do not change with the initial turbulence intensity and it is finally not surprising to observe an increase of the overall effect when the actuation is performed around this preferred mode frequency.

The centreline velocity decay along the streamwise direction is also investigated. The results have
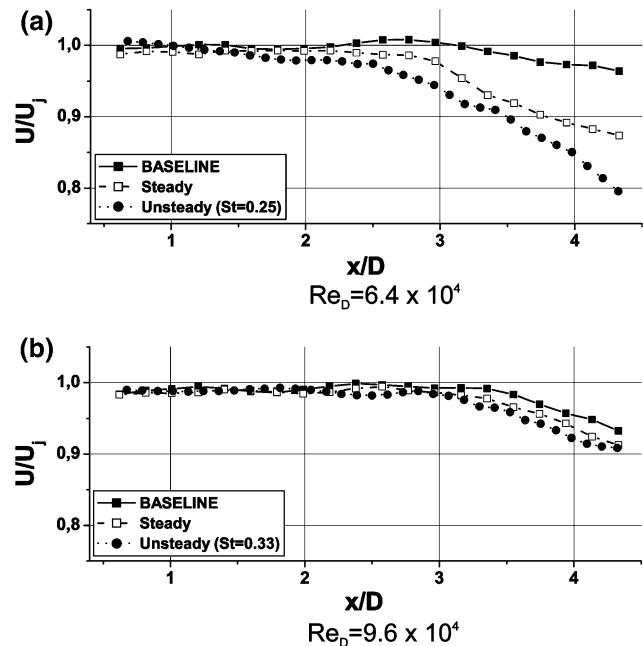
demonstrated that the most effective unsteady actuations are in line with the cross-stream mean velocity profiles and jet width. Indeed, it appears that an actuation at $St = 0.25$ and 0.33 corresponds to the optimized unsteady forcing at $Re_D = 6.4$ and 9.6×10^4, respectively. Figure 22 presents a comparison of the centreline velocity evolution along the x direction for baseline and flow forced by steady and unsteady actuation at optimized frequency. At 20 m/s (Fig. 22a), the unsteady actuation is clearly more effective than the steady one. Indeed, the length of the potential core is shortened (length of about $3D$, $2.7D$ and $2.5D$ for baseline, steady forcing and unsteady forcing, respectively). The decay rate (see Eq. (5)) at the beginning of the centreline velocity reduction (i.e. $3 < x/D < 4.5$) is also enhanced for an unsteady actuation operated at a Strouhal number of 0.25 ($K = 32$, 11 and 7.55 for baseline, steady and unsteady forcing, respectively; note that these values are higher than the ones derived from Fig. 13 due to the shorter x/D range used to compute the K constant).

Compared to a steady actuation, at $Re_D = 9.6 \times 10^4$ the length of the potential core is reduced by 5% when an unsteady actuation is performed at $St = 0.33$. At this Reynolds number, the constant of the decay rate is not improved when an unsteady actuation is applied to the main jet flow ($K \approx 14$).

The centreline evolution confirms that the mixing is improved when an unsteady actuation is proceeded at $St = 0.25$ and 0.33. It also appears that the actuation is

Fig. 23 Centreline TKE evolution at $Re_D = 6.4$ and 9.6×10^4 for jet flow forced by unsteady excitation
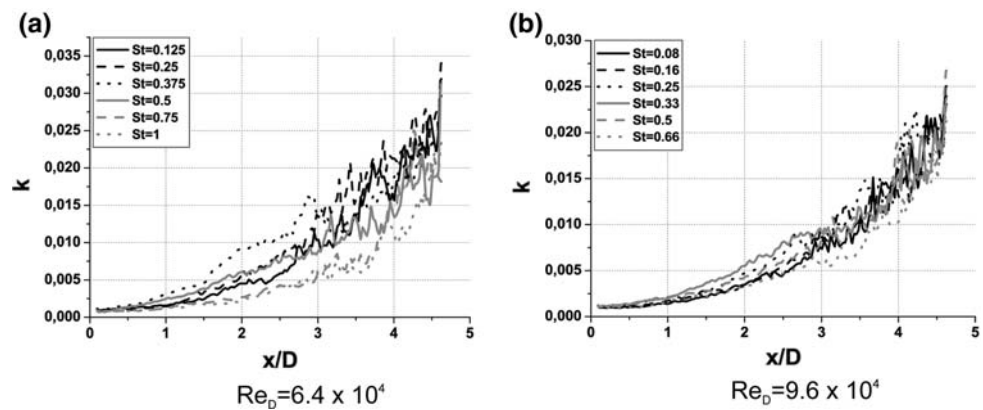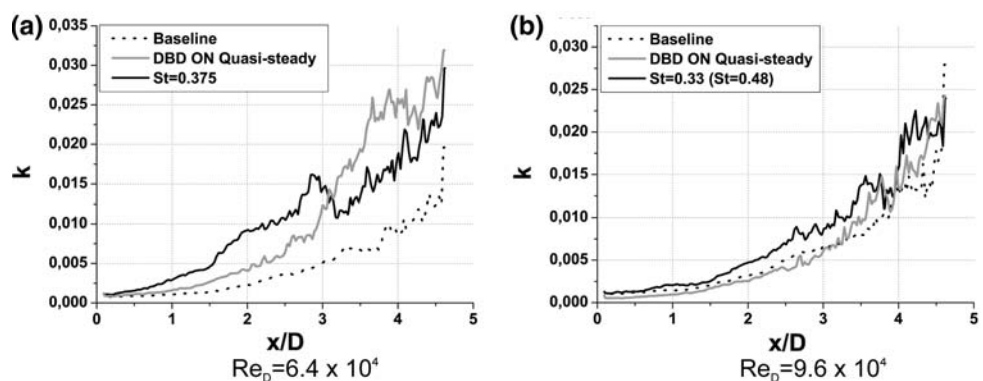

Fig. 24 Comparison of centreline TKE evolution at $Re_D = 6.4$ and 9.6×10^4 for baseline (*dotted lines*), steady (*grey lines*) and unsteady (*black lines*) forcing

less effective when the Reynolds number is increasing as usually observed for turbulent air jets (Raman et al. 1989).

The second parameter related to the mixing enhancement concerns the centreline TKE evolution along the x direction (Fig. 23). These data do not provide a clear demonstration of the existence of a specific frequency inducing an enhancement of the centreline TKE at $z/D = 0$. However, it seems that forcing the flow around $St = 0.3$ is more effective in increasing the centreline TKE for location downstream $x/D = 3$. The interpretation of the results obtained beyond this location is delicate due to important fluctuations in the TKE estimation despite a satisfactory convergence criterion.

Figure 24 summarizes the centreline TKE evolution for baseline flows and flows forced by the quasi-steady and optimized unsteady DBD actuations ($St \approx 0.3$). The first suggestion is that forced flows (by quasi-steady and unsteady forcing) present higher centreline TKE values than the baseline flow over the whole longitudinal acquisition range. The unsteady actuation has greater centreline TKE values up to $x/D = 3$ at $Re_D = 6.4 \times 10^4$ ($x/D = 3.75$ at $Re_D = 9.6 \times 10^4$) and beyond this crossover point, the unsteady actuation generates a lower centreline TKE than a steady one. The unsteady actuation

by double DBDs seems to enhance the centreline TKE only in the near-field region of the jet exit ($x/D < 3$).

However, the major mean flow change occurs in the far-field region as previously reported (Fig. 19c, for instance). The forced flow perturbations initiated at the junction between the jet exit and the diffuser seem to be amplified along the x and y direction. Thus, the integrated values of TKE could be more suitable to demonstrate the ability of the actuator to increase the turbulent energy of the jet flow at $z/D = 0$. For this purpose, the integrated TKE values computed on slices from $x/D = 1$ to 4 are plotted in Fig. 25 for various Strouhal numbers.

The results allow to characterize more accurately the most effective frequency to increase the turbulent energy. The data suggest that forcing around $St = 0.25$ and 0.3 at $Re_D = 6.4 \times 10^4$ and 9.6×10^4, respectively, are more effective for mixing in the region starting from $x/D = 2$ (black lines in figure 25). The results also confirm that the best unsteady actuation (inducing an overall mixing improvement) is performed for St numbers between 0.25 and 0.3. This is in reasonable agreement with data from the literature on the preferred frequency of the jet column instability. The comparison between integrated TKE values for quasi-steady and unsteady actuations demonstrates that the pulsed forcing enhances the turbulent energy at each
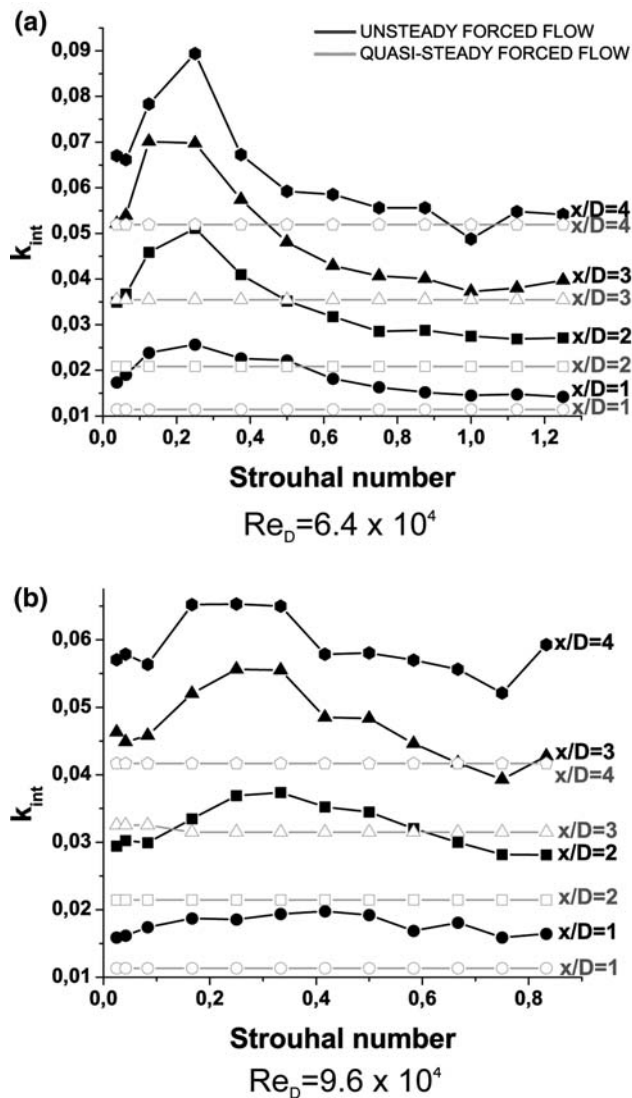
Fig. 25 Integrated TKE at $x/D = 1$, 2, 3 and 4 for primary air jet velocity of 20 m/s (**a**) and 30 m/s (**b**) excited by an unsteady forcing. The *black lines* denote the unsteady forcing while the *grey ones* correspond to the steady forcing

Strouhal number. Nevertheless, at 20 m/s (Fig. 25a), a reduced excitation frequency above 0.9 has limited effects in increasing the TKE.

The increase in turbulence energy is particularly significant at 30 m/s (Fig. 25b), the peak turbulence gain being about 78% (only 49% at $Re_D = 6.4 \times 10^4$). However, the centreline velocity decays at $Re_D = 9.6 \times 10^4$ has demonstrated that the mean effects of the unsteady actuation are limited for high Reynolds numbers. These observations could suggest that an unsteady actuation promotes higher turbulent energy at high Reynolds numbers but the scale of the produced energy may be improper to significantly modify the mean controlled flow. New

experiments are thus required to extend our conclusions to higher Reynolds numbers. A better understanding would certainly emerge from a specific analysis of the turbulent scales following the unsteady excitation by non-thermal plasma discharges in the present configuration.

Here again, the computation of the turbulent Reynolds tensor allows to decompose the contributions of $\overline{u'u'}/U_j^2$ and $\overline{v'v'}/U_j^2$. At $Re_D = 6.4 \times 10^4$, it clearly appears that an excitation at $St = 0.25$ is the most effective unsteady actuation (Fig. 26). In particular, the second diagonal term of the turbulent Reynolds tensor is significantly modified compared to excitations at other frequencies. The momentum transfer due to the velocity fluctuations is largely increased and would result in a mixing enhancement if an unsteady actuation at $St = 0.25$ was performed. At $Re_D = 9.6 \times 10^4$, an increase in the momentum transfer is observed for an excitation at $St = 0.33$, this result being in full agreement with the observations deduced from the computation of the TKE. In this case, the two diagonal terms of the turbulent Reynolds tensor are responsible for this increase. Indeed, an enlargement of the region of high momentum transfer as well as a rise of the non-dimensional levels of both tensor components can be observed. However, a decrease of the control authority is noticed as the Reynolds number gets larger (see the levels of the tensor components at $St = 0.25$ and 0.33 in Figs. 26 and 27, respectively).

4 Concluding remarks

The mixing characteristics of the free shear layer exhausting from a 22-degree-angle diffuser equipped with a control system made of two DBD actuators have been experimentally investigated using PIV measurements. Primary air jet velocities from 10 to 40 m/s are studied (i.e. $Re_D = 3.2$ to 12.8×10^4). Baseline and forced flows are compared at each Reynolds number tested. The mixing is characterized by the potential core length, the centreline TKE, the integrated value of the TKE over various slices along the jet and the turbulent Reynolds stresses. The DBD actuators generate a local flow of approximately 6 m/s along the bevel of the diffuser. This flow is used to attach the naturally separated flow or to presumably control the dynamics of the large eddies initiated at the beginning of the diffuser.

Time-averaged fields results demonstrate that an efficient increase in mixing is performed by a forced flow reattachment along the bevels at $Re_D = 3.2 \times 10^4$, whereas mixing enhancement is potentially realized by the excitation of the coherent structures for higher Reynolds numbers. The actuation introduces streamwise
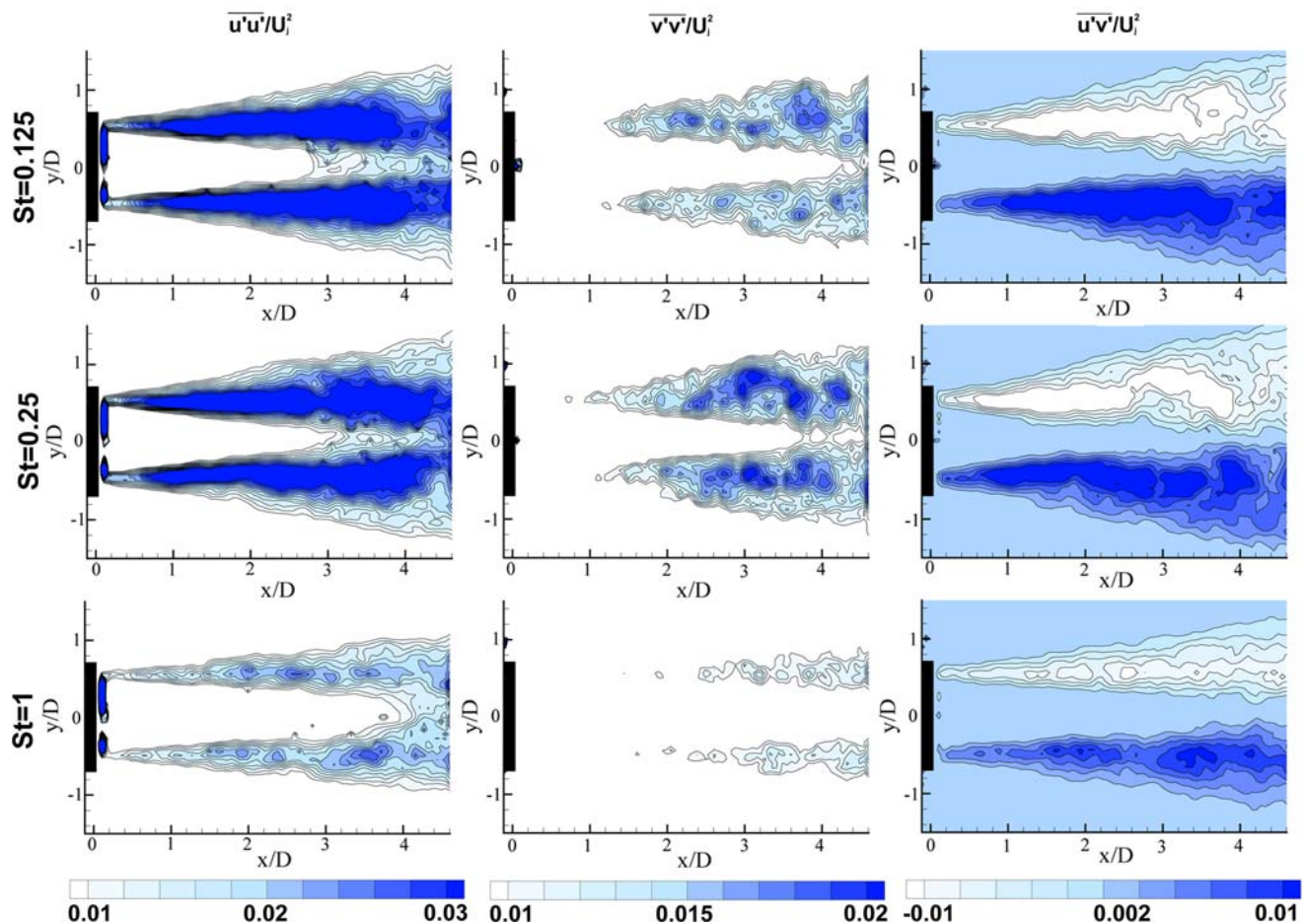
Fig. 26 Turbulent Reynolds stresses for jet flow excited by unsteady actuation ($St = 0.125$, 0.25 and 1) for a centreline velocity U_j of 20 m/s (at $z/D = 0$)

vorticity entraining the higher speed core fluid towards the ambient air. Contrary to tabs, which usually create a pair of counter-rotating vortices, the results concerning the streamwise vorticity ω_x highlight that the DBD actuators produce two pairs of counter-rotating vortices which largely enhance the mixing for primary air jet velocity up to 20 m/s. The TKE is increased up to $x/D = 7$ for jet speed up to lower or equal to 30 m/s (i.e. $Re_D = 9.6 \times 10^4$).

Unsteady actuations over St numbers ranging from 0.08 to 1 were studied. The results suggest that a St number around 0.3 is more effective to enhance the turbulence level in the near-field region. At $Re_D = 6.4 \times 10^4$, the centreline velocity decay is improved and the width of the jet is enlarged when an unsteady excitation is applied at $St = 0.25$. At $Re_D = 9.6 \times 10^4$, unsteady actuations systematically induce a promising increase of the TKE over the reduced frequency range (relative to the baseline and quasi-steady forced flows). It appears that $St = 0.33$ corresponds to the optimized excitation over the Strouhal range investigated here. However, the centreline velocity decay is not clearly enhanced even if a small increase of the jet width is observed for streamwise positions greater than $x/D = 2$.

The excitation provided by the DBD actuators was of typical low amplitude. If this amplitude is not sufficient to force the flow reattachment, the actuation could act on the instability waves in order to phase the coherent structures. However, it seems that low amplitude quasi-steady forcing is ineffective to modify the flow significantly at Reynolds numbers greater than approximately 10^5, especially when the boundary layer is initially turbulent. New experiments need to be performed to demonstrate the ability of DBD actuators to enhance the mixing and change the flow-scale structures by unsteady forcing at primary air jet velocity greater than 30 m/s. Indeed, the level of turbulent energy promoted by an unsteady actuation may be promising if the scale of the turbulent structures can also be controlled at high Reynolds numbers.
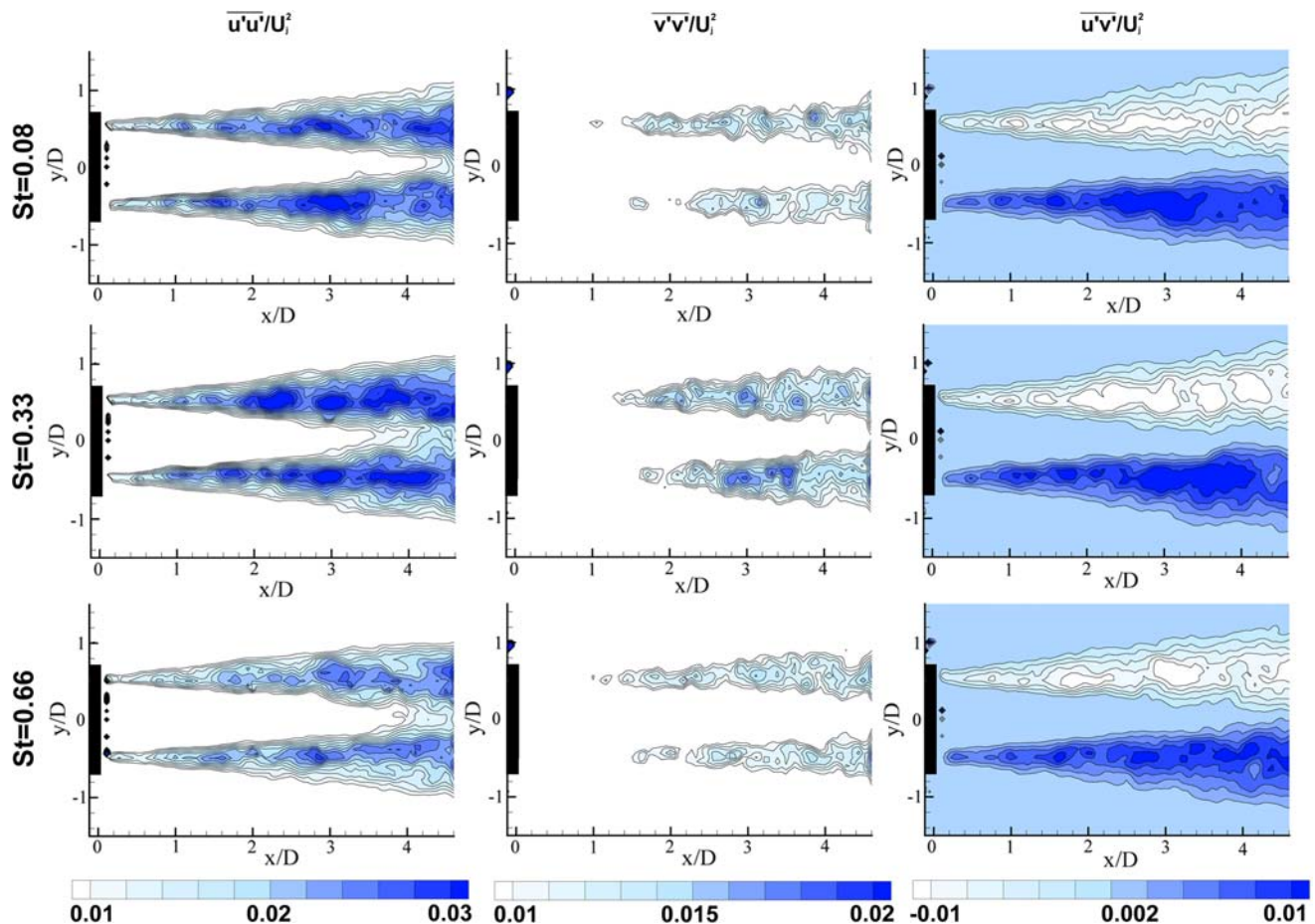
Fig. 27 Turbulent Reynolds stresses for jet flow excited by unsteady actuation ($St = 0.08$, 0.33 and 0.66) for a centreline velocity U_j of 30 m/s (at $z/D = 0$)

References

Benard N, Braud P, Touchard G, Moreau E (2008) Detachment and attachment of an axisymmetric non-reactive jet with turbulent shear layer: control by plasma actuator. Exp Therm Fluid Sci (in press)

Benard N, Jolibois J, Forte M, Touchard G, Moreau E (2007a) Control of an axisymmetric subsonic air jet by plasma actuator. Exp Fluids 43:603–616

Benard N, Braud P, Pons J, Touchard G, Moreau E (2007b) Quasi-steady and unsteady actuation by surface non-thermal plasma discharge for control of a turbulent round air jet. J Turbul 8:1–24

Ben Chiekh M, Bera JC, Sunyach M (2003) Synthetic jet control for flows in a diffuser: vectoring, spreading and mixing enhancement. J Turbul 4:1–12

Boguslawski A, Favre-Marinet M, Abdulwahab A (1999) Jet control by counterflow. Comptes Rendus de l'Académie des Sciences-Series IIB 327:589–595

Braud C, Heitz D, Arroyo G, Perret L, Delville J, Bonnet JP (2004) Low-dimensional analysis, using POD, for two mixing layer-wake interactions. Int J Heat Fluid Flow 25:351–363

Bridges J (2002) Measurements of turbulent flow field in separate flow nozzles with enhanced mixing devices—test report. NASA report 2002–211366

Corke TC, Post ML (2005) Overview of plasma flow control: concepts, optimization and applications. AIAA paper 2005–563

Corke TC, Matlis E (2000) Phased plasma arrays for unsteady flow control. AIAA Paper 2000–2323

Corke TC, Kusek SM (1993) Resonance in axisymmetric jets with controlled helical mode input. J Fluid Mech 249:307–336

Crow SC, Champagne FH (1971) Orderly structure in jet turbulence. J Fluid Mech 48:547–591

Delville J, Collin E, Lardeau S, Lamballais E, Barre S, Bonnet JP (2000) Control of jets by radial fluid injection. ERCOFTAC Bull 44:55–67

Dziomba B, Fiedler H (1985) Effect of initial conditions on two-dimensional free shear layer. J Fluid Mech 152:419–442

Forte M, Jolibois J, Pons J, Moreau E, Touchard G, Cazalens M (2007) Optimization of a dielectric barrier discharge actuator by stationary and non-stationary measurements of the induced flow velocity: application to airflow control. Exp Fluids 43:917–928

Foss JK, Zaman KBMQ (1999) Large and small scale vertical motions in a shear layer perturbed by tabs. J Fluid Mech 382:307–329

Huerre P, Monkewitz PA (1990) Local and global instabilities in spatially developing flows. Ann Rev Fluid Mech 22:473–537

Hussain AKMF, Zaman KBMQ (1981) The 'preferred mode' of the axisymmetric jet. J Fluid Mech 110:39–71

Hussein JH, Capp SP, George WK (1994) Velocity measurements in a high Reynolds number, momentum-conserving, axisymmetric, turbulent jet. J Fluid Mech 258:31–75

Jukes TN, Choi KS (2006) Characterization of surface plasma-induced wall flows trough velocity and temperature measurements. AIAA J 44:764–771

Kurimoto N, Suzuki Y, Kasagi N (2005) Active control of lifted diffusion flames with arrayed micro actuators. Exp Fluids 39:995–1008

Lardeau S, Lamballais E, Bonnet JP (2002) Direct simulation of a jet controlled by fluid injection. J Turbul 3:1–25

Malmström TG, Kirkpatrick AT, Christensen B, Knappmiller KD (1997) Centreline velocity decay measurements in low-velocity axisymmetric jets. J Fluid Mech 246:363–377

Mankbadi RR (1985) The mechanism of mixing enhancement and suppression in a circular jet under excitation conditions. Phys Fluids 28:2062–2074

Mi J, Nathan GJ (1999) Effect of small vortex-generators on scalar mixing in the developing region of a turbulent jet. Int J Heat Mass Transfer 42:3919–3926

Mi J, Nathan GJ, Luxton RE (2000) Centreline mixing characteristics of jets from nine differently shaped nozzles. Exp Fluids 28:93–94

Moreau E (2007) Airflow control by non-thermal plasma actuators. J Phys D Appl Phys 40:605–636

Pack LG, Seifert A (1999) Periodic excitation for jet vectoring and enhanced spreading. AIAA paper 99–0672

Parekh DE, Kibens V, Glezer A, Wiltze JM, Smith DM (1996) Innovative jet flow control: mixing enhancement experiments. AIAA paper 96–0308

Parekh DE, Leonard A, Reynolds WC (1998) Bifurcating jets at high Reynolds numbers. Report TF-35, Stanford University

Post ML, Corke TC (2004) Separation control using plasma actuators—stationary and oscillating airfoils. AIAA paper 2004–0841

Raman G, Zaman KBMQ, Rice EJ (1989) Initial turbulence effect on jet evolution with and without tonal excitation. Phys Fluids A 1:1240–1248

Reeder M, Samimy M (1996) The evolution of a jet with vortex-generating tabs: real-time visualization and quantitative measurements. J Fluid Mech 311:73–118

Roth JR, Sherman DM, Wilkinson SP (1998) Boundary layer flow control with a one atmosphere uniform glow discharge. AIAA Paper 98–0328

Roth JR, Dai X (2006) Optimization of the aerodynamic plasma actuator as an electrohydrodynamic (EHD) electrical device. AIAA paper 2006–1203

Roth JR, Nourgostar S, Bonds TA (2007) The one atmosphere uniform glow discharge plasma (OAUGDP®)—a platform EHD technology for the 21st century. IEEE Trans Plasma Sci 35:233–250

Samimy M, Kastner J, Kim JH, Utkin Y, Adamovich I, Brown C (2004) Development and characterization of plasma actuators for high speed jet control. Exp Fluids 37:577–588

Samimy M, Kim J, Kastner J, Adamovich I, Utkin Y (2007a) Active control of a Mach 0.9 high Reynolds number jet for noise mitigation using plasma actuators. AIAA J 45:890–901

Samimy M, Kim J, Kastner J, Adamovich I, Utkin Y (2007b) Active control of high-speed and high Reynolds number jets using plasma actuators. J Fluids Mech 578:305–330

Strykowski PJ, Wilcoxin RK (1993) Mixing enhancement due to global oscillations in jets with annular counterflow. AIAA J 31:564–570

Suzuki H, Kasagi N, Suzuki Y (2004) Active control of an axisymmetric jet with distributed electromagnetic flap actuators. Exp Fluids 36: 498–509

Winant CD, Browand FK (1974) Vortex pairing: the mechanism of turbulent mixing layer growth at moderate Reynolds number. J Fluid Mech 63:237–255

Zaman KBMQ, Hussain AKMF (1980) Vortex pairing in a circular jet under controlled excitation, part one, general jet response. J Fluid Mech 101:449–491

Zaman KBMQ, Reeder M, Samimy M (1994) Control of an axisymmetric jet using vortex generators. Phys Fluids 6:778–793

Zaman KBMQ, Raman G (1997) Reversal in spreading of a tabbed circular jet under controlled excitation. Phys Fluids 9:3733–3741